2014

A Discontinuous Galerkin Chimera scheme

Marshall C. Galbraith
School of Aerospace Systems

John A. Benek
Aerospace Systems Directorate

Paul D. Orkwis
School of Aerospace Systems

Mark G. Turner
School of Aerospace Systems

A Discontinuous Galerkin Chimera scheme

CrossMark

Marshall C. Galbraith [a,*], John A. Benek [b], Paul D. Orkwis [a], Mark G. Turner [a]

[a] University of Cincinnati, School of Aerospace Systems, Cincinnati, OH 45221, United States
[b] U.S. Air Force Research Laboratory, Aerospace Systems Directorate, Wright-Patterson Air Force Base, OH 45433, United States

ARTICLE INFO

ABSTRACT

The Chimera overset method is a powerful technique for modeling fluid flow associated with complex engineering problems using structured meshes. The use of structured meshes has enabled engineers to employ a number of high-order schemes, such as the WENO and compact differencing schemes. However, the large stencil associated with these schemes can significantly complicate the inter-grid communication scheme and hole cutting procedures. This paper demonstrates a methodology for using the Discontinuous Galerkin (DG) scheme with Chimera overset meshes. The small stencil of the DG scheme makes it particularly suitable for Chimera meshes as it simplifies the inter-grid communication scheme as well as hole cutting procedures. The DG-Chimera scheme does not require a donor interpolation method with a large stencil because the DG scheme represents the solution as cell local polynomials. The DG-Chimera method also does not require the use of fringe points to maintain the interior stencil across inter-grid boundaries. Thus, inter-grid communication can be established as long as the receiving boundary is enclosed by or abuts the donor mesh. This makes the inter-grid communication procedure applicable to both Chimera and zonal meshes. Details of the DG-Chimera scheme are presented, and the method is demonstrated on a set of two-dimensional inviscid flow problems.

Published by Elsevier Ltd.

1. Introduction

The Chimera overset method has been used successfully in many applications since it was first introduced for the Euler equations in 1983 [1]. The Chimera method uses a set of structured overlapping grids to define the computational domain. Using a set of overlapping grids enables modeling of complex geometries that otherwise could not be meshed with a single structured grid [2]. It also allows users to "hot swap" geometric features without having to remesh the entire geometry of interest. The method has also been shown to be useful for modeling geometries in relative motion, such as store separation [3,4] or rotorcraft blades [5,6].

The overset grid system defines a set of overlapping computational subdomains. The boundaries of the subdomains that are interior to the computational domain and do not coincide with the domain boundary are called artificial boundaries. For finite volume and finite difference schemes, additional points exterior to the artificial boundaries are required to maintain the interior difference stencil. These points are called fringe points; they form a fringe exterior to the subdomains. Fringe points in a Chimera overset scheme are equivalent to ghost points used to maintain

the interior stencil across grid boundaries in a multi-block scheme [7,8]. The difference is that fringe points are explicitly included in the grid system during the grid generation process, whereas ghost points are generated implicitly created during an initialization process and are coincident with points in the neighboring grids. The values of the dependent variables at the fringe points are obtained by interpolation from neighboring grids. The interpolation provides the coupling mechanism between the overset grids. Sufficient overlap between grids is required for proper interpolation to the fringe points. Insufficient overlap can result in reduced order of accuracy in the interpolation or a failure to establish proper interpolation. Fringe points without proper interpolation are often denoted as orphan points [9,10]. The grid system must be adjusted if orphan points are present, typically in a manual fashion, until no orphan points exist.

The structured meshes in the Chimera method have facilitated the application of high-order schemes to complex geometries. High-order schemes have proven to be particularly useful for Large Eddy Simulation calculations [11–14] and have the potential to reduce numerical discretization errors and reduce computation time for steady flow problems relative to 1st- and 2nd-order accurate methods [15]. However, high-order schemes, such as compact differencing [16,11] and WENO [17,18], require large stencils. These large stencils require additional fringes associated with the

* Corresponding author. Tel.: +1 937 255 3761.
E-mail address: Marshall.Galbraith@gmail.com (M.C. Galbraith).

Nomenclature

DOF	degrees of freedom
$\vec{F}$	Euler Flux Tensor
$\vec{\mathcal{F}}$	polynomial expansion of the Euler Flux Tensor
Γ_e	spatial boundary of the cell e
Γ_t	temporal boundary of the cell e
M_∞	reference mach number
N	spatial polynomial order of the solution approximation
N_{GQ}	number of gauss quadrature nodes used for a artificial boundaries
N_g	spatial polynomial order of a cell geometric mapping
N_t	temporal polynomial order of the solution approximation
Ω_e	volume domain of the cell e
P_n	nth-order one-dimensional legendre polynomial
Q	conservative variable vector
V	velocity vector $[u, v]$
$\vec{X}$	cartesian node (x,y)
α	angle of attack
γ	ratio of specific heats
h	representative cell size ($sqrt(1/DOF)$)
$\vec{n}$	spatial cell boundary normal vector
$\vec{n}_t$	temporal cell boundary normal vector
p	pressure
ϕ	roe dissipation vector
ψ	polynomial test function
ρ	density
ρE	total energy

ρu, ρv	cartesian momentum components in x, and y directions
s	cell face local curvilinear coordinate
t	temporal dimension
u, v	cartesian velocity components in x, and y directions
x, y	cartesian coordinates
ξ, η, τ	cell local curvilinear coordinates
$\Delta \dot{m}$	mass flux error, $(\dot{m}_{out} - \dot{m}_{in})/\dot{m}_{in}$
η_e	number of faces of a cell
C	airfoil chord length
C_d	lift coefficient, $D/(Cq_\infty)$
C_l	lift coefficient, $L/(Cq_\infty)$
C_p	pressure coefficient $(P - P_\infty)/0.5$
C_x	horizontal force coefficient, $F_x/(Cq_\infty)$
C_y	vertical force coefficient, $F_y/(Cq_\infty)$
D	drag
F_x	horizontal force
F_y	vertical force
h_x, h_y	cartesian cell bounding box dimensions
L	lift
q_∞	reference dynamic pressure $\frac{1}{2}\rho \vec{V}^2$
Δ	increment
∇	gradient vector, $\left(\frac{\partial}{\partial x}, \frac{\partial}{\partial y}\right)$
$\|u\|$	L^2-norm, $\sqrt{\sum u_i^2}$
$-, +$	cell boundary interior and exterior values

---

artificial boundaries in order to maintain the stencil of the high-order scheme [19]. The additional fringe points increase the possibility of the grid system having orphan points. The larger stencils can also cause significant complications when performing hole cutting and grid partitioning for parallel calculations [20]. Furthermore, the high-order schemes need to be paired with interpolation schemes of equal order [21]. These high-order interpolation schemes also require large stencils, which can complicate the generation of meshes with appropriate overlapping regions that do not generate orphan points [20].

The Discontinuous Galerkin (DG) scheme is a high-order accurate discretization scheme that is receiving growing interest. The method was originally developed for the first order neutron transport problem [22], and was later extended to non-linear transport equations [23]. The scheme represents the approximate solution using local polynomials that are continuous within a given cell, but the approximation is allowed to be discontinuous across cell faces. Most importantly, in the context of Chimera overset meshes, the DG discretization has a stencil that only depends on the current cell and its immediate neighbors. Hence, hole cutting can be performed without the significant grid overlap restrictions imposed on high-order finite volume and finite difference methods. A large interpolation stencil is not required for inter-grid communication, because the higher-order information is retained within the polynomial representation of the approximate solution. In addition, the inter-grid communication method presented here does not require fringe points to maintain the interior scheme on artificial boundaries and naturally reduces to the scheme of the interior faces for the case of coincident abutting faces. Hence, a DG-Chimera grid system is always valid so long as no physical gaps exist between the grids.

Details of the DG-Chimera communication interface are presented, and the DG-Chimera method is used to compute subsonic, transonic, and supersonic flows for both internal an external geometries. Flow fields computed using overlapping grids compare well with single grid solutions of comparable resolution. A small error in mass flux is observed similar to traditional finite volume and finite difference Chimera schemes that rely on a discrete interpolation of the conservative variables [24–28]. However, calculations of inviscid channel flow with a smooth bump are used here to demonstrate that the DG-Chimera scheme maintains the proper order of accuracy despite these errors. This has also been demonstrated for finite volume Chimera schemes based on discrete interpolation [29]. The mass flux errors are also consistent, i.e., they go to zero with mesh refinement and/or increase in the order of the polynomial approximation.

2. Governing equations

The governing equations employed in this work are the Euler equations, which can be written in the divergence, or conservative form in two-dimensions as

$$\frac{\partial Q}{\partial t} + \nabla \cdot \vec{F} = 0, \tag{1}$$

where the conservative variables are $Q = [\rho, \quad \rho u, \quad \rho v, \quad \rho E]^T$, the inviscid fluxes are

$$\vec{F}(Q) = \left[\begin{pmatrix} \rho u \\ \rho u^2 + p \\ \rho uv \\ \rho u H \end{pmatrix}, \begin{pmatrix} \rho v \\ \rho vu \\ \rho v^2 + p \\ \rho v H \end{pmatrix} \right], \tag{2}$$

$H = \frac{\rho E + p}{\rho}$ is the total enthalpy, and

$$p = (\gamma - 1)\left(\rho E - \frac{\rho}{2}(u^2 + v^2)\right), \tag{3}$$

is the static pressure. An artificial viscosity term is added to Eq. (1) to mitigate fluctuations in the solution in the vicinity of shocks when they are present. The method was developed by Barter and

Darmofal, and details of the artificial viscosity formulation can be found in Refs. [30–32]. The modified Euler equations that include the artificial viscosity are

$$\frac{\partial Q}{\partial t} + \nabla \cdot \vec{F} - \nabla \cdot \vec{F}^{av} = 0, \tag{4}$$

where

$$\vec{F}^{av}(Q, \nabla Q) = \left[\begin{pmatrix} \hat{\epsilon} \frac{h_x}{h} \frac{\partial \rho}{\partial x} \\ \hat{\epsilon} \frac{h_x}{h} \frac{\partial \rho u}{\partial x} \\ \hat{\epsilon} \frac{h_x}{h} \frac{\partial \rho v}{\partial x} \\ \hat{\epsilon} \frac{h_x}{h} \frac{\partial \rho H}{\partial x} \end{pmatrix}, \begin{pmatrix} \hat{\epsilon} \frac{h_y}{h} \frac{\partial \rho}{\partial y} \\ \hat{\epsilon} \frac{h_y}{h} \frac{\partial \rho u}{\partial y} \\ \hat{\epsilon} \frac{h_y}{h} \frac{\partial \rho v}{\partial y} \\ \hat{\epsilon} \frac{h_y}{h} \frac{\partial \rho H}{\partial y} \end{pmatrix} \right], \tag{5}$$

Note that the gradient of the total enthalpy can be expressed in terms of the conservative variables and their gradients as

$$\nabla \rho H = \nabla \rho E + \frac{\partial p}{\partial \rho} \nabla \rho + \frac{\partial p}{\partial \rho u} \nabla \rho u + \frac{\partial p}{\partial \rho v} \nabla \rho v + \frac{\partial p}{\partial \rho E} \nabla \rho E. \tag{6}$$

The artificial viscosity coefficient, $\hat{\epsilon}$, is a limited value of ϵ that is governed by the non-linear Poisson equation

$$\frac{\partial \epsilon}{\partial t} = \nabla \cdot \left(\left[\frac{\eta}{\tau} \right] \nabla \epsilon \right) + \frac{1}{\tau} \left(\frac{\bar{h}}{N} \lambda_{max} \tilde{s}_k - \epsilon \right), \tag{7}$$

where

$$\begin{aligned} \tau &= \frac{h_{min}}{c_1 N \lambda_{max}}, \\ \left[\frac{\eta}{\tau} \right] &= \frac{c_1 c_2 N \lambda_{max}}{h_{min}} \begin{bmatrix} h_x^2 & 0 \\ 0 & h_y^2 \end{bmatrix}, \\ \lambda_{max} &= \sqrt{u^2 + v^2} + \sqrt{\frac{\gamma p}{\rho}}, \\ \bar{h} &= \frac{1}{2}(h_x + h_y), \\ h_{min} &= min(h_x, h_y), \\ c_1 &= 3, \\ c_1 c_2 &= 15. \end{aligned} \tag{8}$$

Here, h_x and h_y are the extents of the bounding box of a cell. The term $\tilde{s}_k$ in the source term of Eq. (7) is a limited value of the shock sensor s_k expressed as

$$\tilde{s}_k = \begin{cases} 0 & s_k \leqslant s_0 - \kappa \\ \frac{1}{2}\epsilon_0 \left(1 + sin\left(\frac{1}{2} \frac{\pi(s_k - s_0)}{\kappa}\right)\right) & s_0 - \kappa < s_k \leqslant s_0 + \kappa \\ \epsilon_0 & s_0 + k < s_k \end{cases} \tag{9}$$

The value of s_k is given by a modified version of the resolution indicator [33] as

$$s_k = log_{10} \left(\frac{\int_{\Omega_e} (p_{11} - p_{00})^2 d\Omega}{\int_{\Omega_e} p_{11}^2 d\Omega} \right), \tag{10}$$

where $p_{11} = \sum_{i=0}^{N-1} \sum_{j=0}^{N-1} p_{ij} \psi_{ij}$ is the linear polynomial expansion of pressure, and p_{00} is the cell mean pressure value. The expression for obtaining $\hat{\epsilon}$ by limiting ϵ is

$$\hat{\epsilon} = \begin{cases} 0 & \epsilon \leqslant \hat{\epsilon}_{low} \\ \frac{1}{2}\hat{\epsilon}_{hi}\left(1 + sin\left(\pi\left[\frac{\epsilon - \hat{\epsilon}_{low}}{\hat{\epsilon}_{hi} - \hat{\epsilon}_{low}} - \frac{1}{2}\right]\right)\right) & \hat{\epsilon}_{low} < \epsilon \leqslant \hat{\epsilon}_{hi} \\ \hat{\epsilon}_{hi} & \hat{\epsilon}_{hi} < \epsilon \end{cases}$$

$$\hat{\epsilon}_{low} = 0.01 \lambda_{max} \frac{\bar{h}}{N}, \tag{11}$$

$$\hat{\epsilon}_{hi} = \lambda_{max} \frac{\bar{h}}{N}.$$

3. Discontinuous Galerkin method

The approach to solving Eq. (1) is the Discontinuous Galerkin (DG) method. In this approach, the conservative variables and flux vectors are expressed as an expansion in cell local polynomial basis functions $\psi \in P_{\Omega_e}^N$

$$Q(\xi, \eta) = \sum_{i=0}^{N} \sum_{j=0}^{N} Q_{ij} \psi_{ij}(\xi, \eta), \tag{12}$$

$$\vec{\mathcal{F}}(\xi, \eta) = \sum_{i=0}^{N} \sum_{j=0}^{N} \vec{\mathcal{F}}_{ij} \psi_{ij}(\xi, \eta), \tag{13}$$

$$\vec{\mathcal{F}}^{av}(\xi, \eta) = \sum_{i=0}^{N} \sum_{j=0}^{N} \vec{\mathcal{F}}_{ij}^{av} \psi_{ij}(\xi, \eta), \tag{14}$$

where Q_{ij}, $\vec{\mathcal{F}}_{ij}$, and $\vec{\mathcal{F}}_{ij}^{av}$ are the modal coefficients in the polynomial expansion, N is the order of the polynomial expansion, and $\xi \in [-1, 1]$, and $\eta \in [-1, 1]$ are curvilinear coordinates local to each cell. A tensor product of the one-dimensional orthogonal Legendre polynomials [34], P, is chosen as the test and basis functions, i.e. $\psi_{ij}(\xi, \eta) = P_i(\xi)P_j(\eta)$. The flux vector expansion in Eq. (13) is an L^2-approximation of the exact polynomial expansion $\vec{F}(Q(\xi, \eta))$, i.e. $\vec{\mathcal{F}}(\xi, \eta) \approx \vec{F}(Q(\xi, \eta))$. As the Legendre polynomials are orthogonal, the coefficients of the flux vector expansion are computed as

$$\vec{\mathcal{F}}_{ij} = \frac{\int_{\Omega_e} \psi_{ij}(\xi, \eta)\vec{F}(Q(\xi, \eta))d\Omega}{\int_{\Omega_e} \psi_{ij}^2(\xi, \eta)d\Omega}. \tag{15}$$

Excluding the time dependent term, Eq. (4) are put in weak form by multiplying them by the set of test functions $\psi = [\psi_{ij}]^T$, $\forall i, j \in [0, N]$, and applying Gauss's theorem to obtain

$$\int_{\Gamma_e} \psi \vec{\mathcal{F}} \cdot \vec{n} d\Gamma - \int_{\Omega_e} \nabla \psi \cdot \vec{\mathcal{F}} d\Omega - \int_{\Gamma_e} \psi \vec{\mathcal{F}}^{av} \cdot \vec{n} d\Gamma + \int_{\Omega_e} \nabla \psi \cdot \vec{\mathcal{F}}^{av} d\Omega = 0. \tag{16}$$

The boundary integrals flux terms are computed from values on both sides of the cell boundary. This provides the mechanism to couple the solution across cell boundaries. The inviscid fluxes are computed using the Roe approximate Riemann solver [35]. The boundary and volume integrals associated with the artificial viscosity flux are modified by adding the lifting operator, $\vec{r}$, in accords with the BR2 discretization scheme [36]. The final discrete weak form of Eq. (4) is

$$\begin{aligned} R(Q) = &\int_{\Gamma_e} \psi \left[\frac{1}{2}\left(\vec{\mathcal{F}}(Q^+) + \vec{\mathcal{F}}(Q^-)\right) \cdot \vec{n} - \frac{1}{2}\phi(Q^+, Q^-)|\vec{n}| \right] d\Gamma \\ &- \int_{\Omega_e} \nabla \psi \cdot \vec{\mathcal{F}}(Q)d\Omega - \int_{\Gamma_e} \psi \frac{1}{2}\left(\vec{\mathcal{F}}^{av}(Q^+, \nabla Q^+ + \eta_e \vec{r}^+)\right. \\ &+ \vec{\mathcal{F}}^{av}(Q^-, \nabla Q^- + \eta_e \vec{r}^-)\left.\right) \cdot \vec{n} d\Gamma + \int_{\Omega_e} \nabla \psi \cdot \left(\vec{\mathcal{F}}^{av}\left(Q, \nabla Q + \vec{R}\right)\right) d\Omega = 0, \end{aligned} \tag{17}$$

where the $-$, $+$ superscripts indicate cell interior and exterior values respectively and $\phi(Q^+, Q^-)$ is the dissipation flux. The lifting operator is defined by the boundary integral over a single face, Γ_k, of the cell as

$$\int_{\Omega_e} \psi \vec{r}_k d\Omega = \int_{\Gamma_k} \psi \frac{1}{2}(Q^+ - Q^-)\vec{n} d\Gamma. \tag{18}$$

Hence, there are four lifting operators, $\vec{r}_k$, for a quadrilateral cell. $\vec{R}$ is the sum of the lifting operators $\vec{r}_k$ on the cell. A more detailed description of the discretization and solver can be found in Ref. [37].

4. Grid polynomial mapping

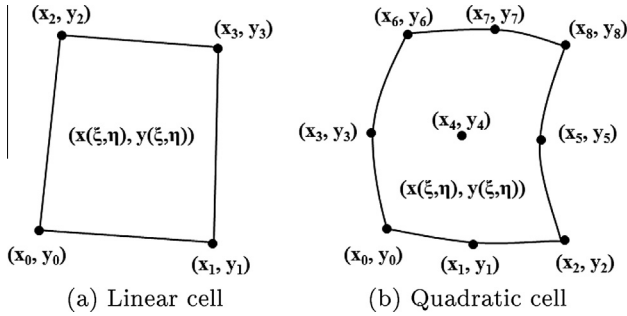The DG solver presented in this work is formulated for structured meshes. These meshes can be generated using a

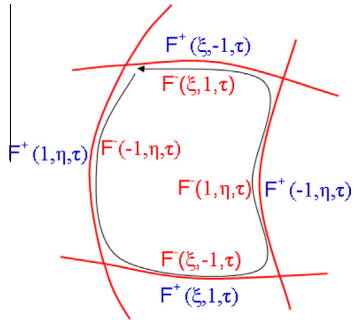Fig. 1. Nodal representation of a linear and quadratic cell.

(a) Linear cell (b) Quadratic cell

Fig. 2. Interior boundary integration.

Fig. 3. Overlapping grids.

traditional structured mesh generator. The solver generates cell local polynomial representations, $(x(\xi,\eta), y(\xi,\eta))$, of the cell coordinates. The geometric polynomial mapping of the cell coordinates is formulated as a sum involving the same test functions, ψ, as used in the DG discretization of the governing equations. Hence,

$$x(\xi,\eta) = \sum_{i=0}^{N_g}\sum_{j=0}^{N_g} x_{ij}\psi_{ij}(\xi,\eta),$$

$$y(\xi,\eta) = \sum_{i=0}^{N_g}\sum_{j=0}^{N_g} y_{ij}\psi_{ij}(\xi,\eta),$$

(19)

where x_{ij} and y_{ij} are the coefficients of the geometric polynomial mapping, N_g is the order of the geometric polynomial mapping, and $\psi_{ij}(\xi,\eta) = P_i(\xi)P_j(\eta)$. The coefficients are found by equating the expansion with the associated cell nodal values. For example, the following system of equations is solved to find the coefficients of $x(\xi,\eta)$ for the linear cell shown in Fig. 1a.

$$\begin{pmatrix} \psi_{00}(-1,-1) & \psi_{10}(-1,-1) & \psi_{01}(-1,-1) & \psi_{11}(-1,-1) \\ \psi_{00}(1,-1) & \psi_{10}(1,-1) & \psi_{01}(1,-1) & \psi_{11}(1,-1) \\ \psi_{00}(-1,1) & \psi_{10}(-1,1) & \psi_{01}(-1,1) & \psi_{11}(-1,1) \\ \psi_{00}(1,1) & \psi_{10}(1,1) & \psi_{01}(1,1) & \psi_{11}(1,1) \end{pmatrix}\begin{pmatrix} x_{00} \\ x_{10} \\ x_{01} \\ x_{11} \end{pmatrix} = \begin{pmatrix} x_0 \\ x_1 \\ x_2 \\ x_3 \end{pmatrix},$$

(20)

The same process is repeated for the y coordinate to obtain the complete polynomial mapping of the cell. Additional cell nodes are required to establish a higher-order polynomial representation. For example, a quadratic cell requires nine nodal values as shown in Fig. 1b. Hence, a grid size of $m \times n$ cells requires $(N_g m + 1) \times (N_g n + 1)$ nodes.

5. Artificial boundaries

The inter-grid communication method is designed to maintain the interior discretization scheme on artificial boundaries. For an interior cell, the boundary integral of the inviscid terms from Eq. (17) is evaluated on all boundaries where the fluxes $\vec{\mathcal{F}}(Q^-)$, $\vec{\mathcal{F}}(Q^+)$, and the dissipation flux, $\phi(Q^+,Q^-)$, are evaluated using the trace of the dependent variables taken from the cell interior and from neighboring cells as shown in Fig. 2. For an artificial boundary, the exterior conservative variables, Q^+, must be provided by one, or multiple, cells from overlapping meshes. The two overlapping grids shown in Fig. 3 are used as an example to show how the exterior conservative

(a) Red Face Mapping (b) Gauss-Quadrature Nodes in the Blue Mesh
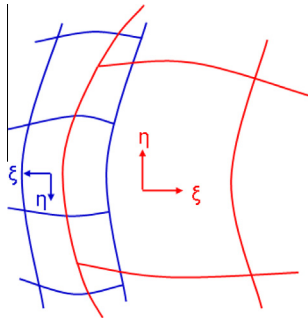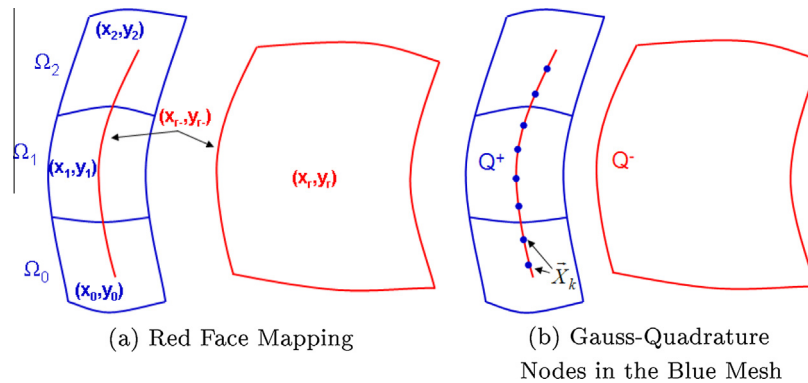
Fig. 4. Obtaining conservative variables from the blue mesh. (For interpretation of the references to color in this figure legend, the reader is referred to the web version of this article.)

(a) Linear Elements with Coincident Nodes

(b) Miss-matched Linear Elements with Linear Interface

(c) Linear Elements with Coincident Nodes of Convex Quadratic Elements
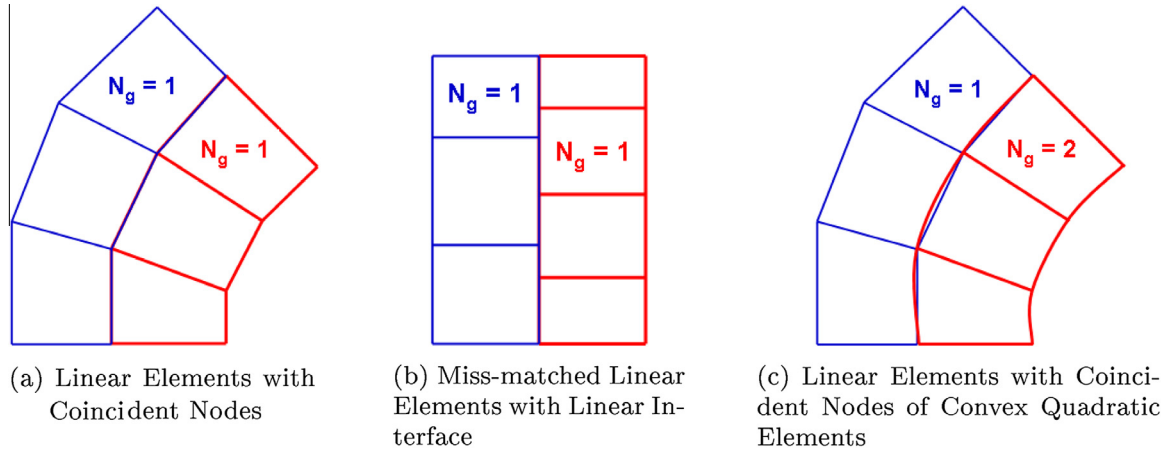
Fig. 5. Sufficient overlap for zonal type interfaces.

variables are obtained for the boundary integral on the left boundary of the red[1] cell.

The left face of the red cell, defined by the coordinate mappings $x_r(-1, \eta)$ and $y_r(-1, \eta)$, $\eta \in [-1, 1]$ (see Fig. 4a), is seeded with Gauss-Quadrature (GQ) nodes to integrate the red mesh solution polynomial and obtain Q^+ from the blue cells. The polynomial mappings $x_r(-1, \eta)$ and $y_r(-1, \eta)$ are then used to obtain the Cartesian coordinate, $\vec{X}_k = (x_r(-1, s_k), y_r(-1, s_k))$, that corresponds to the Gauss-Quadrature node, $s_k \in [-1, 1]$. The Cartesian coordinate, $\vec{X}_k$, is then used to obtain the corresponding cell local coordinates, $\left(\xi\left(\vec{X}_k\right), \eta\left(\vec{X}_k\right)\right)$, in the cells of the blue mesh as shown in Fig. 4b.

A Kd-tree [38] search algorithm is used to determine which GQ nodes are located within the bounding box of each blue cell Ω_i. GQ nodes that reside inside the bounding box of the cell Ω_i may or may not reside inside the cell Ω_i. To determine that the GQ node $\vec{X}_k$ is located within a cell Ω_i, the local curvilinear coordinate location, $\left(\xi_i(\vec{X}_k), \eta_i(\vec{X}_k)\right)$, corresponding to $\vec{X}_k$ is found using Newton's method

$$\begin{pmatrix} \frac{\partial}{\partial \xi} x_i(\xi^n, \eta^n) & \frac{\partial}{\partial \eta} x_i(\xi^n, \eta^n) \\ \frac{\partial}{\partial \xi} y_i(\xi^n, \eta^n) & \frac{\partial}{\partial \eta} y_i(\xi^n, \eta^n) \end{pmatrix} \begin{pmatrix} \Delta \xi \\ \Delta \eta \end{pmatrix} = \begin{pmatrix} -(x_i(\xi^n, \eta^n) - x_r(-1, s_k)) \\ -(y_i(\xi^n, \eta^n) - y_r(-1, s_k)) \end{pmatrix},$$
(21)

where

$$\begin{aligned} \xi^0 &= 0, \\ \eta^0 &= 0, \\ \xi^{n+1} &= \xi^n + \Delta \xi, \\ \eta^{n+1} &= \eta^n + \Delta \eta. \end{aligned}$$

It is possible for the Newton method to diverge even though the node is located within the cell if either ξ^{n+1} or η^{n+1} exceed the valid range of $[-1, 1]$. Thus, both ξ^{n+1} and η^{n+1} are limited to the range $[-1, 1]$ after each iteration. The Newton solver is stopped when the L^2-norm of the right hand side of Eq. (21) drops below a tolerance of 1e−10, or the Newton method reaches a maximum number of 20 iterations. The cell Ω_i is a donor cell for the coordinate $\vec{X}_k$ if the L^2-norm drops below the tolerance of 1e−10. If the L^2-norm is above the required tolerance after 20 iterations, the coordinate $\vec{X}_k$ is deemed to reside outside of the cell Ω_i, and Ω_i is discarded as a

donor for the coordinate $\vec{X}_k$. The choice of 20 iterations is a balance between providing enough iterations for the Newton method to converge and maintaining a reasonable execution time when the node resides outside of the cell. The average nodal value is used if multiple donor cells exist for a given Gauss-Quadrature node. The simple average has worked thus far on all cases considered, and a more sophisticated method for choosing the appropriate donor when multiple exist is left for future work. For stationary grids, this process of locating cell local curvilinear coordinates is performed once during an initialization stage.

The cell local curvilinear coordinates corresponding to $\left(\xi_i(\vec{X}_k), \eta_i(\vec{X}_k)\right)$ are used to obtain nodal Q^+ values that correspond to $\vec{X}_k$. The coefficients for the modal representation of Q^+ are then obtained using the following inner product

$$Q^+ = \sum_{j=0}^{N} q_j^+ \psi_j \qquad where$$
$$q_j^+ = \frac{\sum_{k=0}^{N_{GQ}} w_k \psi_j(s_k) Q_i\left(\xi_i(\vec{X}_k), \eta_i(\vec{X}_k)\right)}{\int_{-1}^{1} \psi_j^2(s) ds} \qquad \forall j \in [0, N].$$
(22)

where w_k are the Gauss-Quadrature integration weights. The modal representation of Q^+ is then used to evaluate the inviscid flux term of Eq. (17). A numerical approximation is introduced in Eq. (22) by using a single set of Gauss-Quadrature nodes to integrate the nodal Q^+ values across cell boundaries without regard to possible discontinuities in the approximation across cell boundaries. These errors can be reduced, but not eliminated, by increasing the number of Gass-Quadrature nodes. Numerical experiments, presented in the results section, indicate that increasing Gauss-Quadrature node count beyond $N_{GQ} = \lceil 3N/2 \rceil + 1$ does not significantly reduce the error.

The modal coefficients for the gradient ∇Q^+ is also obtained using Fig. 5a for the viscous terms in the artificial dissipation in Eq. (17). However, no cell exterior to the artificial boundary is available to perform the volume integral to obtain $\vec{r}^+$. Thus, as an approximation, $\vec{r}^-$ is used in place of $\vec{r}^+$ in Eq. (17). This is equivalent to assuming that an exterior cell exists of equal volume to the interior cell. This is similar to how Dirichlet boundary conditions are imposed in the BR2 discretization [36].

It is important to note that unlike standard overset methods the communication method for the DG-Chimera method has no requirement on the extent of overlap; only that the grids overlap or abut. In the special case where the face of the red cell is coinci-

---

[1] For interpretation of color in Figs. 3 and 6, the reader is referred to the web version of this article.

(a) Miss-matched Linear Elements with Curved Interface

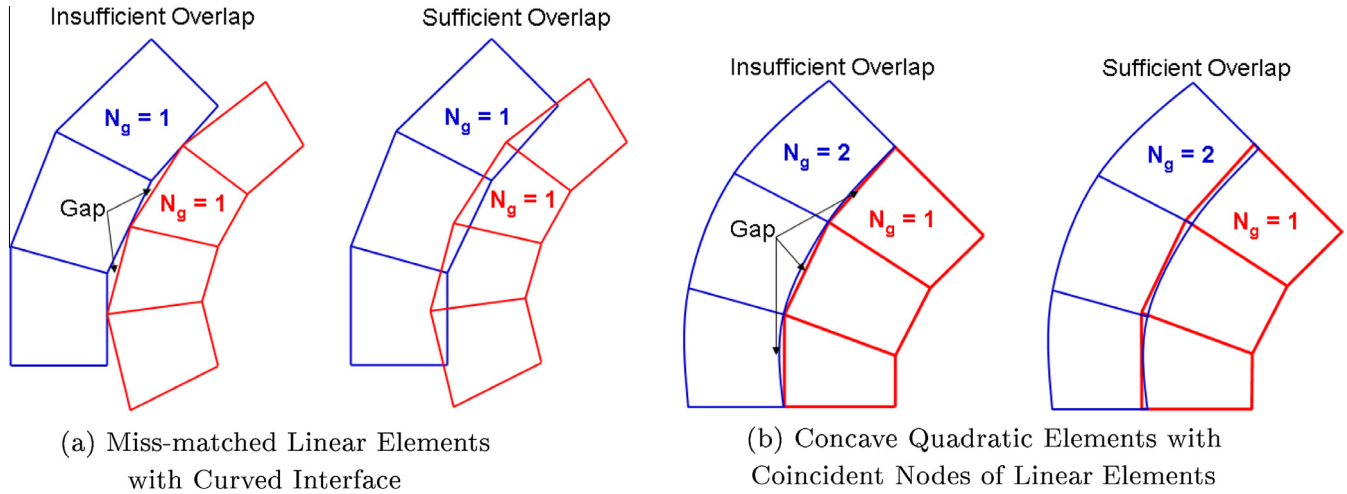(b) Concave Quadratic Elements with Coincident Nodes of Linear Elements

Fig. 6. Sufficient overlap type interfaces and corrections for sufficient overlap.

dent with the face of one of the blue cells (Fig. 4), the inter-grid communication for the advection flux reduces naturally to that of the interior scheme. Thus, mesh boundaries on a set of zonal meshes [39] will naturally use the interior scheme, as shown in Fig. 5a and b, for the advective fluxes. There is still an approximation in the diffusion terms as a result of using the BR2 discretization scheme. However, the results show that this approximation is acceptable.

The method is also independent of the order of the geometric cell mapping of the two meshes. The communication scheme can connect two meshes consisting of linear cells, or quadratic and higher cells. Information can also be transferred between two meshes that do not use the same order of the geometric mapping as shown in Fig. 5c. However, gaps cannot exist between two meshes, i.e., they must overlap or abut. Two examples of using a zonal type interface that lead to gaps between meshes are shown in Fig. 6. As shown in Fig. 6a, two linear meshes that do not have coincident nodes along a curved artificial boundary may produce gaps between the meshes. The gap can be removed by adjusting the meshes so that the boundaries overlap. In Fig. 6b, the red mesh consists of cells with a quadratic geometric mapping and the blue mesh cells use a linear geometric mapping. In this case, even though the nodes on the common boundary are coincident, gaps are produced between the meshes as the faces of linearly mapped cells on the red mesh are secants to the curved boundary. Again, the gaps can be removed by overlapping the boundaries between the two meshes. Gaps are detected when no suitable donor cell is found for one or more GQ receiver nodes. When gaps are detected, the grids must be regenerated without gaps.

6. Convergence to a steady state

A Quasi-Newton method is used to obtain the steady state solution of Eq. (17). A complete linearization of Eq. (17), (including the artificial boundaries), along with a psuedo-time term is used to form the system of linear equations on the entire domain Ω,

$$\int_{\Omega_e} \psi \frac{\Delta Q}{\Delta t_e} d\Omega + \frac{\partial R(Q^n)}{\partial Q} \Delta Q = -R(Q^n), \qquad (23)$$

that must be solved for each Quasi-Newton iteration, n. The pseudo-time term is an approximation to the linearization of the time term and limits the step size of the Quasi-Newton solver by adding a diagonal mass matrix to the linearization of $R(Q)$. The mass matrix

is diagonal due to the orthogonality of the Legendre polynomials. Only the mean value of the coordinate transformation Jacobian is used in the integration of the pseudo-time term. The mean value is convenient to use as it is the first coefficient in a Legendre polynomial expansion. The solution at iteration $n+1$ is obtained with $Q^{n+1} = Q^n + \Delta Q$. The local time step, Δt_e, is computed for each cell using a *CFL* number

$$\Delta t_e = \frac{CFL^n h_e}{\bar{\lambda}_e},$$

where $h_e = \sqrt{\Omega_e}$, $\bar{\lambda}_e = |\bar{V}_e| + \bar{c}_e$ is the cell mean characteristic speed, and $|\bar{V}_e|$, $\bar{c}_e$ are the cell mean flow speed and speed of sound respectively. The *CFL* number is increased each Quasi-Newton iteration, as proposed by Orkwis and McRae [40], with the formula

$$CFL^n = CFL^0 \frac{\left\| R(Q^0) \right\|}{\left\| R(Q^n) \right\|}, \qquad (24)$$

where $CFL^0 = 10$. Thus, the Quasi-Newton solver will approach a Newton solver as $CFL \to \infty$.

The system of linear equations for the Quasi-Newton method is solved at each iteration using a flexible version of the GMRES iterative matrix solution algorithm, FGMRES [41]. A Block Incomplete-LU preconditioner with one level of fill in (ILU1) is used to accelerate the FGMRES algorithm [41]. The GMRES solver is converged to a tolerance of 1e−12 on each Quasi-Newton iteration, and the solution is considered converged when $\|R(Q^n)\|$ drops below 1e−10.

7. Results

This section presents results of applying the DG-Chimera scheme to a selection of inviscid flow problems: a subsonic channel flow with a Gaussian smooth bump, a turbomachinery cascade in subsonic flow, a transonic channel flow with a 10% circular arc, a supersonic normal shock in a diffuser, the SKF 1.1 airfoil [42] in subsonic and transonic flow, and a circular cylinder in supersonic flow. These flow problems demonstrate that the DG-Chimera scheme is applicable for both internal and external flow problems ranging from subsonic to supersonic flows. The channel flow with a Gaussian smooth bump is used to characterize the numerical approximations associated with the artificial boundaries. The turbomachinery cascade blade demonstrates that the artificial bound-
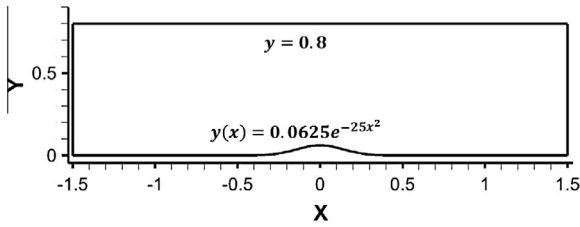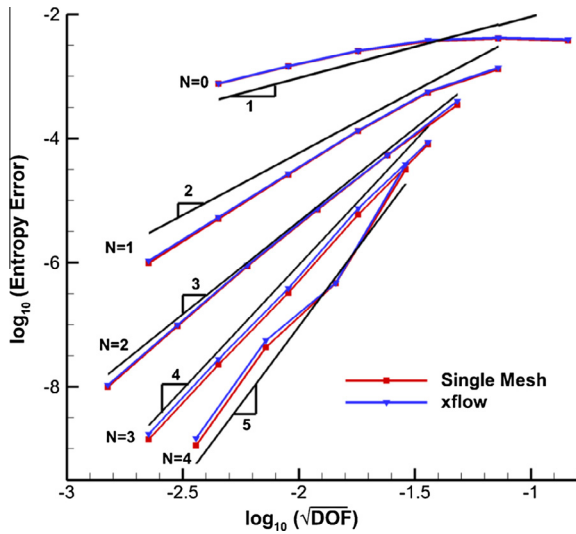
Fig. 7. Smooth bump geometry.

Fig. 8. Smooth bump spatial order of accuracy verification with XFLOW.

aries do not introduce significant errors when applied to internal flows with a high degree of turning. The transonic channel flow with a 10% bump and super-sonic diffuser flow with a shock demonstrate that the DG-Chimera scheme is able to capture shocks that cross the artificial boundaries in an internal flow. Flow fields computed using the SKF 1.1 airfoil demonstrate that the DG-Chimera scheme is applicable to external sub-sonic and transonic flows. The Mach 2 cylinder is used to demonstrate that the artificial boundaries do not introduce significant errors when a strong shock crosses the artificial boundaries. These flow problems were selected specifically because they can be meshed with a single grid. The single grid solution is then used as a reference for a comparison with a Chimera mesh with comparable grid resolution. The results demonstrate that the flow fields computed using the Chimera meshes are nearly identical to the flow fields computed using the single grids for $N \geq 1$. Two additional flow problems are presented: the SKF 1.1 airfoil with a flap and an isentropic convecting vortex. The SKF 1.1 airfoil with a flap is a more complex geometry that cannot be meshed with a single structured meshes and is more representative of the traditional use of Chimera meshes. The convecting vortex flow problem demonstrates that the high-order discretization is better able to maintain the vortex pressure deficit relative to a lower-order discretization with a given number of degrees of freedom.

Cubic and quartic polynomial expansions are used for grid cells that represent the geometry. The use of curved elements to represent geometry was shown to be necessary by Bassi and Rebay [43] for high-order of accuracy.

7.1. Gaussian smooth bump

Channel flow with a Gaussian smooth bump [15] is used to verify the solver order of accuracy both with and without Chimera artificial boundaries, as well as to assess errors introduced by using GQ integration in Eq. (22) that spans multiple donor cells. The computational domain of the channel is defined in Fig. 7. Slip wall boundary conditions are imposed by enforcing $\vec{V} \cdot \vec{n} = 0$ on the upper and lower boundaries. The pressure for the slip wall boundary conditions is the pressure from the interior cell evaluated on the wall. The left inflow boundary specifies total pressure and temperatures corresponding to $M_\infty = 0.5$, as well as a zero flow angle. A constant back pressure is applied to the right outflow boundary. A uniform quadrilateral grid with a quartic, $N_g = 4$, polynomial mapping is used to compare the entropy error, defined as
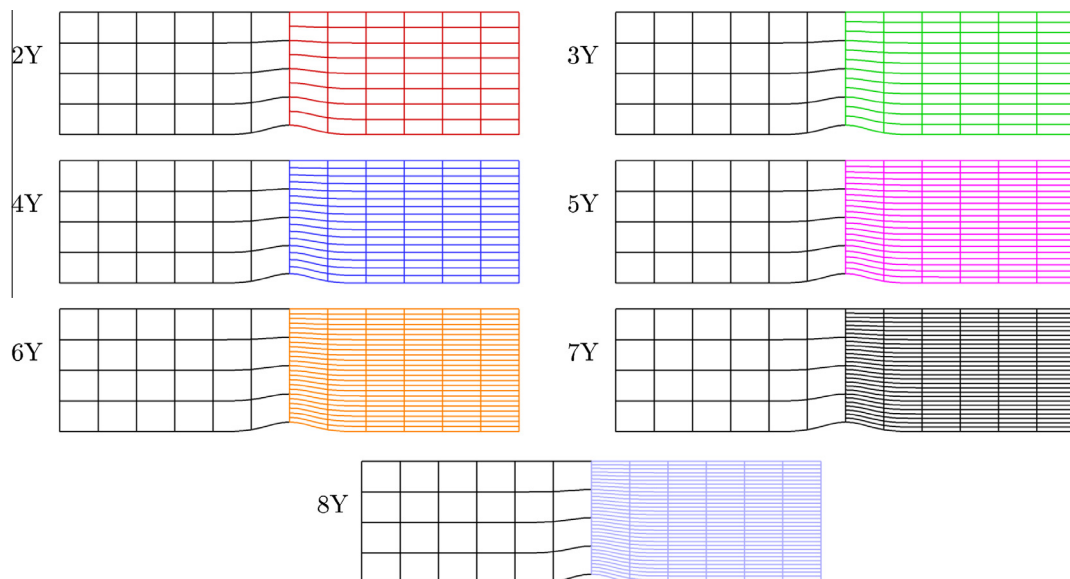

Fig. 9. Smooth bump zonal meshes.

$$Entropy\ Error = \sqrt{\frac{\int \left(\frac{\frac{p}{\rho^\gamma} - \frac{p_\infty}{\rho_\infty^\gamma}}{\frac{p_\infty}{\rho_\infty^\gamma}}\right)^2 d\Omega}{\int d\Omega}},\qquad(25)$$

with numerical solutions obtained using Fidkowski et al.'s [44] XFLOW code, which also utilizes a Discontinuous Galerkin discretization. A comparison of the entropy error for the two codes with increasing mesh refinement and increasing order of approximation is shown in Fig. 8. The entropy error decreases with the expected order of accuracy of $N + 1$ and agrees well with values obtained with XFLOW.

A series of grids where the computational domain is divided in two, an upstream and downstream domain with an interface at $x = 0$, are used to assess the number of GQ nodes required to evaluate the integral in Eq. (22). Both the upstream and downstream domains are meshed with uniform quadrilateral grids. These are zonal meshes [39] since the upstream and downstream grids do not overlap. The downstream grids have 2–8 times as many cells in the vertical direction as the upstream grid. The meshes are labeled, $2Y$–$8Y$ to denote the ratio of cells between the downstream and upstream grids and are illustrated for the coarsest upstream grid in Fig. 9. The convergence history of the Quasi-Newton method for the 8Y series of grids with $N_{GQ} = \lceil 3N/2 \rceil + 1$ is shown in Fig. 10. This figure illustrates that near quadratic convergence of the residual is achieved for most grids and order of accuracy despite the presence of the artificial boundary. This behavior is not typical of most artificial boundary formulations, which usually rely on explicit updates of the artificial boundaries. The entropy error computed using the zonal meshes for increasing mesh resolution and order of approximation are shown with three different GQ node counts in Fig. 11. Using the $\sqrt{DOF}$ for the horizontal in Fig. 11 would cause the curves to shift horizontally due to the increased number of downstream cells in the grids. Instead, the horizontal cell size, h_x, is used to clarify the figure. Despite the sudden change in cell size, the correct order of accuracy of $N + 1$ in the en-
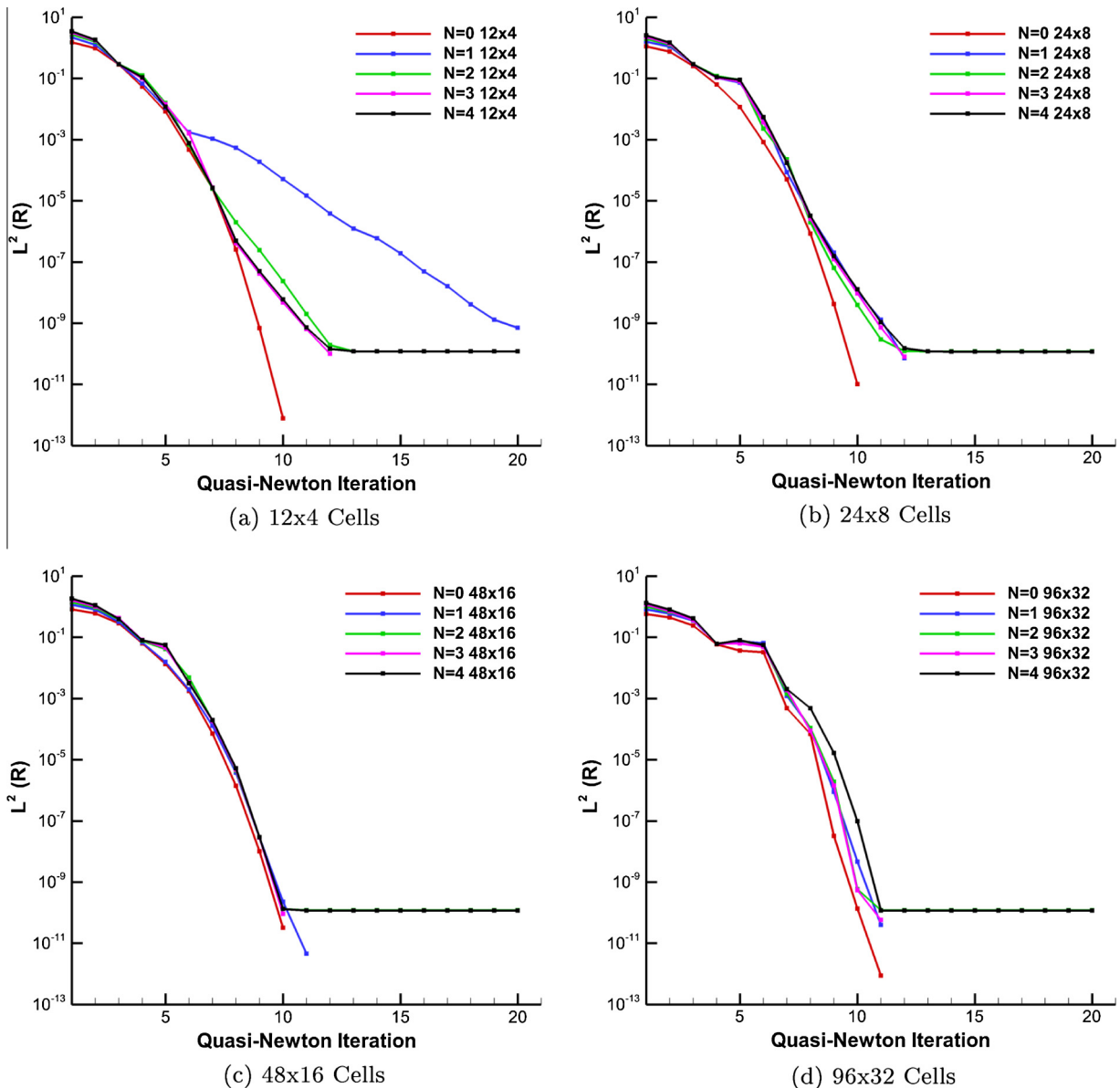

(a) 12x4 Cells

(b) 24x8 Cells

(c) 48x16 Cells

(d) 96x32 Cells

Fig. 10. Convergence history for the 8Y smooth bump zonal meshes and $N_{GQ} = \lceil 3N/2 \rceil + 1$ (Cell counts correspond to a 1Y mesh).

(a) $N_{GQ} = N + 1$
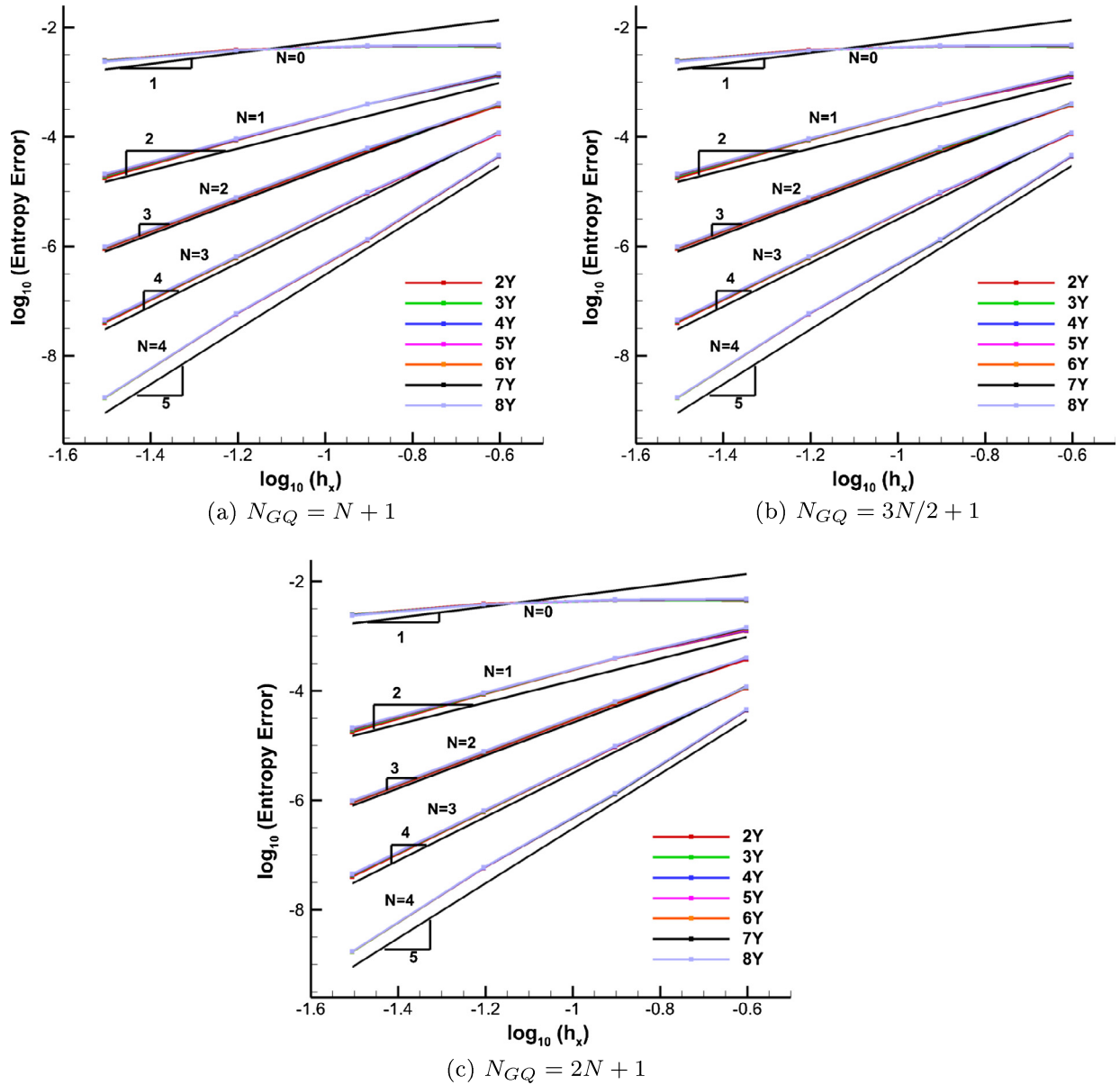

(b) $N_{GQ} = 3N/2 + 1$

(c) $N_{GQ} = 2N + 1$

Fig. 11. Observed order of accuracy using the zonal meshes with different number of quadrature nodes.

tropy error is maintained regardless of the ratio in vertical cell count or the number of GQ nodes. The effect of the numerical approximations of the zonal interface are characterized by the difference in mass flux between the inflow and outflow boundaries.

The mass flux at both boundaries is computed using the same fluxes used to impose the boundary conditions. The mass flux errors for the zonal meshes are shown in Fig. 12. These results are used to assess the appropriate number of GQ nodes required to minimize the mass flux errors. Each plot shows the mass flux error for a given polynomial approximation, N, and GQ node count, N_{GQ}, with increasing cell refinement for the 2Y–8Y meshes. The order of the polynomial approximation increases down the rows of plots, and the GQ node count increases across the columns. In general, the mass flux error decreases with increase in the polynomial approximation and/or increase in GQ nodes. This behavior demonstrates that the mass flux error of the DG-Chimera scheme is consistent for all orders of accuracy. The mass flux error tends to decreases when the GQ node count is increased from

$N_{GQ} = N + 1$ to $N_{GQ} = \lceil 3N/2 \rceil + 1$. There is less of a reduction in the mass flux error when going from $N_{GQ} = \lceil 3N/2 \rceil + 1$ to $N_{GQ} = 2N + 1$. Hence, a GQ node count of $N_{GQ} = \lceil 3N/2 \rceil + 1$ is deemed adequate based on this study. No real trend is observed between the meshes with different vertical cell count ratios.

For the next comparison, the computational domain is divided into three parts: upstream and downstream domains, and a domain centered at $x = 0$. The meshes for the upstream and downstream domains have the same cell count, but the center domain has twice the number of cells in the vertical direction. Both zonal and Chimera meshes are used to grid the three domains. The center grid in the zonal mesh does not overlap the upstream and downstream grids, whereas the center grid in the Chimera mesh overlaps the upstream and downstream grids by a half cell width as shown in Fig. 13. The entropy errors computed from a single grid, the zonal mesh, and the Chimera mesh are shown in Fig. 14. The entropy errors computed using the zonal and Chimera meshes is comparable to those computed on the single grid. Most
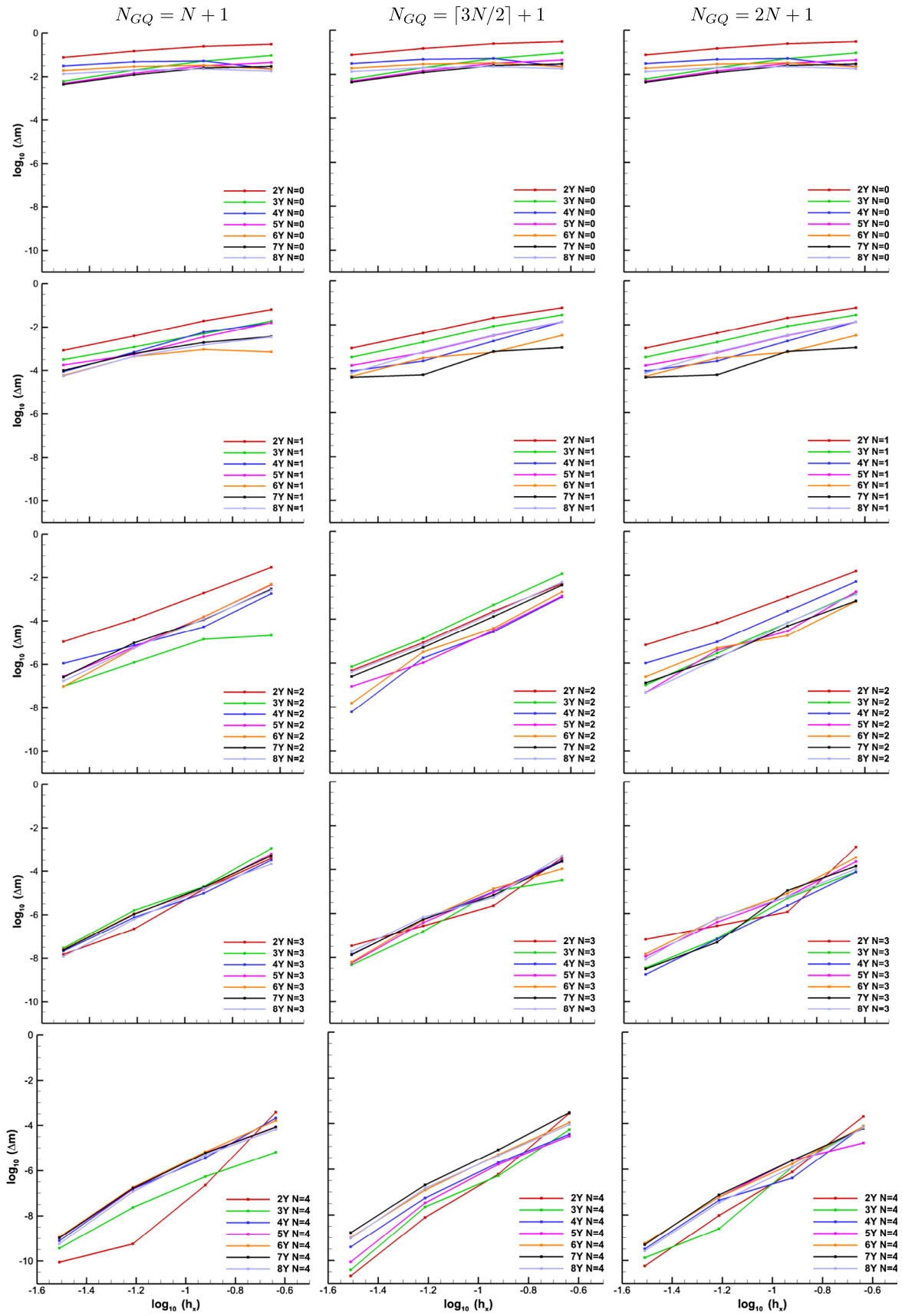
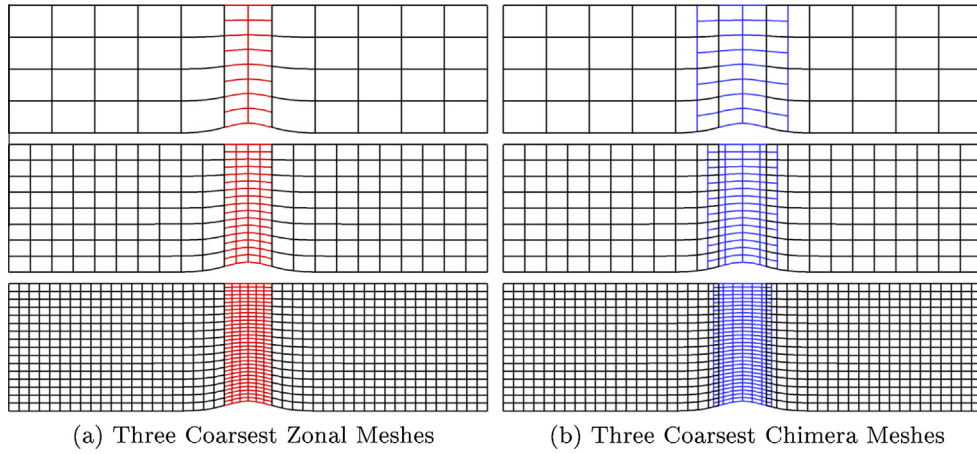**Fig. 12.** Smooth bump zonal mesh mass flux error.

(a) Three Coarsest Zonal Meshes   (b) Three Coarsest Chimera Meshes

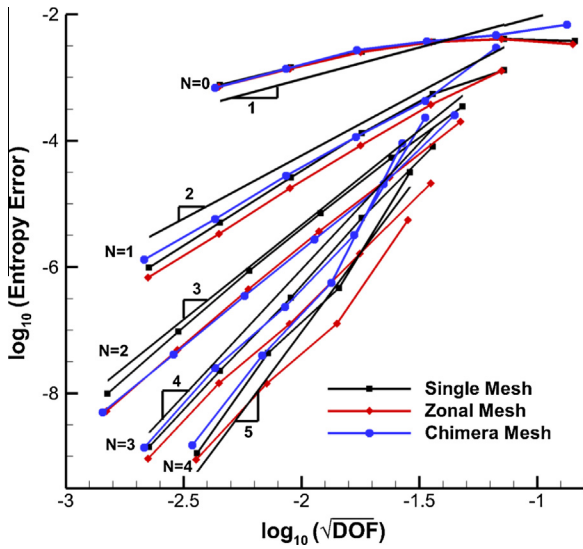**Fig. 13.** Smooth bump with 3 grids.

Fig. 14. Smooth bump spatial order of accuracy with 3 grids.

importantly, the proper $N + 1$ order of accuracy is observed on all three meshes. The mass flux error computed using both the zonal and Chimera meshes also tends towards zero for increased grid resolution and increased order of approximation as shown in Fig. 15.

7.2. Turbomachinery cascade

A turbomachinery cascade is used to demonstrate the DG-Chimera scheme on an internal subsonic flow problem with a high degree of turning. The cascade blade geometry has a 35° leading edge metal angle and a 100° turning angle. The maximum thickness to chord ratio is 16.35% and the blade-to-blade spacing to axial chord ratio is 0.898, which yields a Zweifel [45,46] loading coefficient of 1.06. The blade shape is defined by a quartic B-Spline thickness distribution and a cubic B-Spline meanline curvature distribution that is integrated twice to give the meanline. A zonal mesh with coincident nodes on all interfaces, shown in Fig. 16a, is used to compute a reference flow field. The Chimera mesh, shown in Fig. 16b, uses the grid from the zonal mesh that defines
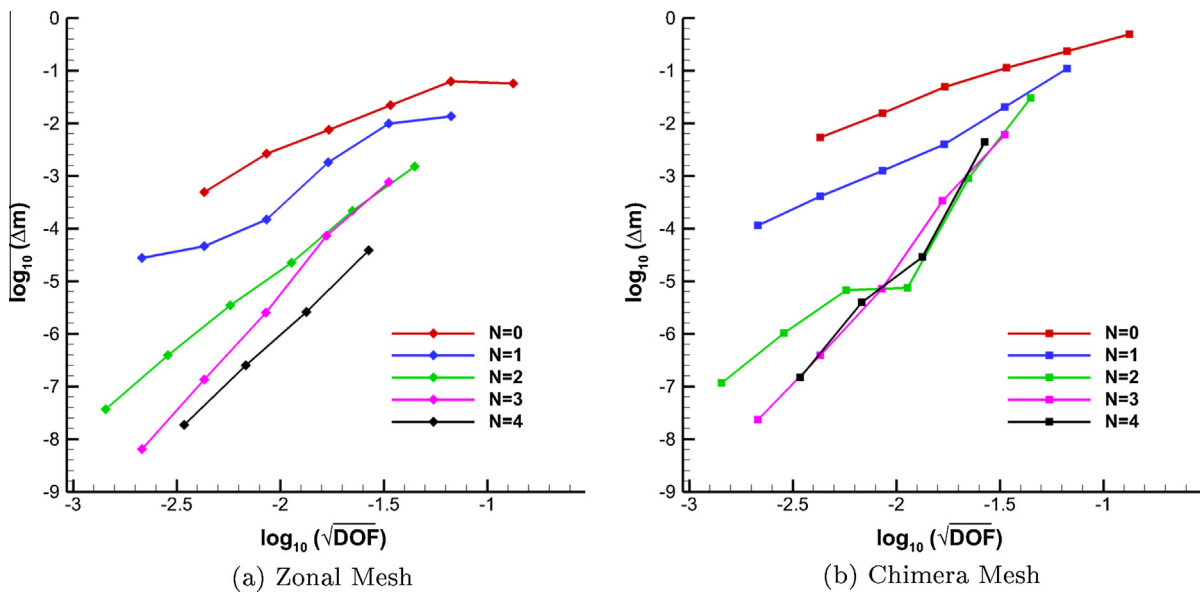

(a) Zonal Mesh   (b) Chimera Mesh

Fig. 15. Smooth bump with 3 grids mass flux error.

(a) Zonal Mesh, 1962 Cells

(b) Chimera Mesh, 2089 Cells
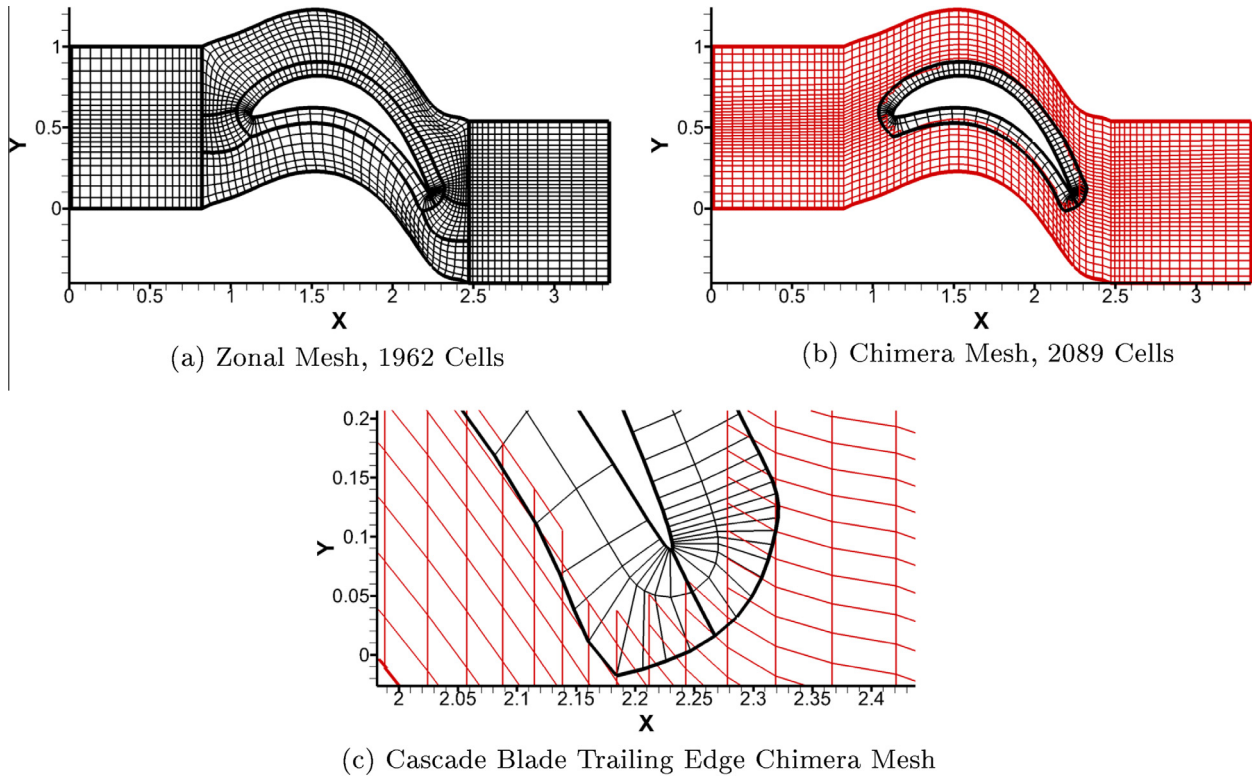

(c) Cascade Blade Trailing Edge Chimera Mesh

Fig. 16. Turbomachinery cascade blade meshes.

the surface of the cascade blade and a single background grid with the same point distribution along the upper and lower boundaries as the zonal mesh. The region of the background grid that would otherwise reside inside the cascade rotor has been excluded from the computational domain using a "hole-cutting" procedure [47]. Note that the grid representing the blade only has two cells normal to the wall and the cell size differs significantly near the trailing edge as shown in Fig. 16c. A periodic boundary is used to connect the upper and lower boundaries of the computational domain. Total pressure and temperature corresponding to $M_\infty = 0.25$ and a ratio of velocity components of $v/u = 0.5$ is enforced at the inflow boundary to ensure the proper flow angle. A fixed static back pressure with a fixed outlet to inlet static pressure ratio of $P_{out}/P_{in} = 0.8853$ is imposed at the outflow boundary. The Cartesian force coefficients, mass averaged outflow angle, β, difference in mass flux between the inlet and exit boundaries, surface pressure coefficient, and pressure coefficient contours are given in Fig. 17 with increasing order of approximation. The Cartesian force coefficients and mass averaged outflow angle computed using the two meshes agree well for $N \geq 1$. The mass flux error for the zonal mesh are machine zero, and the mass flux error tends to decrease for the Chimera mesh with increase in the order of approximation. The mass flux error does increase sightly when the order of approximation increases from $N = 2$ to $N = 3$. This type of behavior is also observed in the mass flux errors computed on the Chimera grid for the inviscid channel flow with a smooth bump (see Fig. 15b), were the mass flux error with $N = 2$ is sometimes lower than with $N = 3$. Surface pressure coefficient and pressure coefficient contours computed using the two meshes agree well for $N = 1$, and are indistinguishable for $N \geq 2$.

7.3. Channel flow with 10% circular arc

This case demonstrates the DG-Chimera scheme on an internal transonic flow with a shock [48,25,28]. A single grid and a Chimera

overset mesh for a channel flow with a circular arc on the lower wall are shown in Fig. 18. The circular arc has a unit length and extends 10% of the channel height. Total pressure and temperature boundary conditions are imposed at the inflow. A fixed back pressure condition is imposed on the right exit boundary. Zero mass flux through the upper and lower boundaries is enforced with a slip wall boundary condition. An inflow Mach number of $M_\infty = 0.675$ is chosen to produce a transonic shock on the downstream portion of the arc. The difference in mass flux, the lower surface pressure coefficient, and pressure coefficient contours are shown in Fig. 19 for increasing order of the approximating polynomial. The mass flux error tends to decrease with increased order of the polynomial approximation, though more gradually than the sub-sonic flows. In addition, for $N \geq 1$, the surface pressure coefficient and pressure coefficient contours agree well between the single grid and the Chimera mesh. Differences in the surface pressure can be attributed to the different topology of the two meshes. For the single grid, the grid lines align with the shock, whereas the grid lines on the surface of the arc for the Chimera mesh do not.

7.4. Normal shock in a diffuser

A diffuser test case is used to demonstrate the DG-Chimera scheme on an internal supersonic flow with a normal shock. The single grid and Chimera overset mesh with linear cell mappings for the diffuser are shown in Fig. 20. The diffuser expands at a $10°$ angle on the upper and lower surfaces. The grids at the inflow and outflow boundaries in the Chimera mesh are used to integrate the mass flux over a non-overlapping boundary. A supersonic inflow with $M_\infty = 1.1$ is imposed on the inflow boundary. A fixed back pressure computed from the normal shock equations [49] for a normal shock with an upstream Mach number of 1.1 is imposed on the outflow boundary. The mass flux error, surface pressure coefficient from the lower wall, and pressure coefficient contours are shown in Fig. 21. The mass flux error between the in-
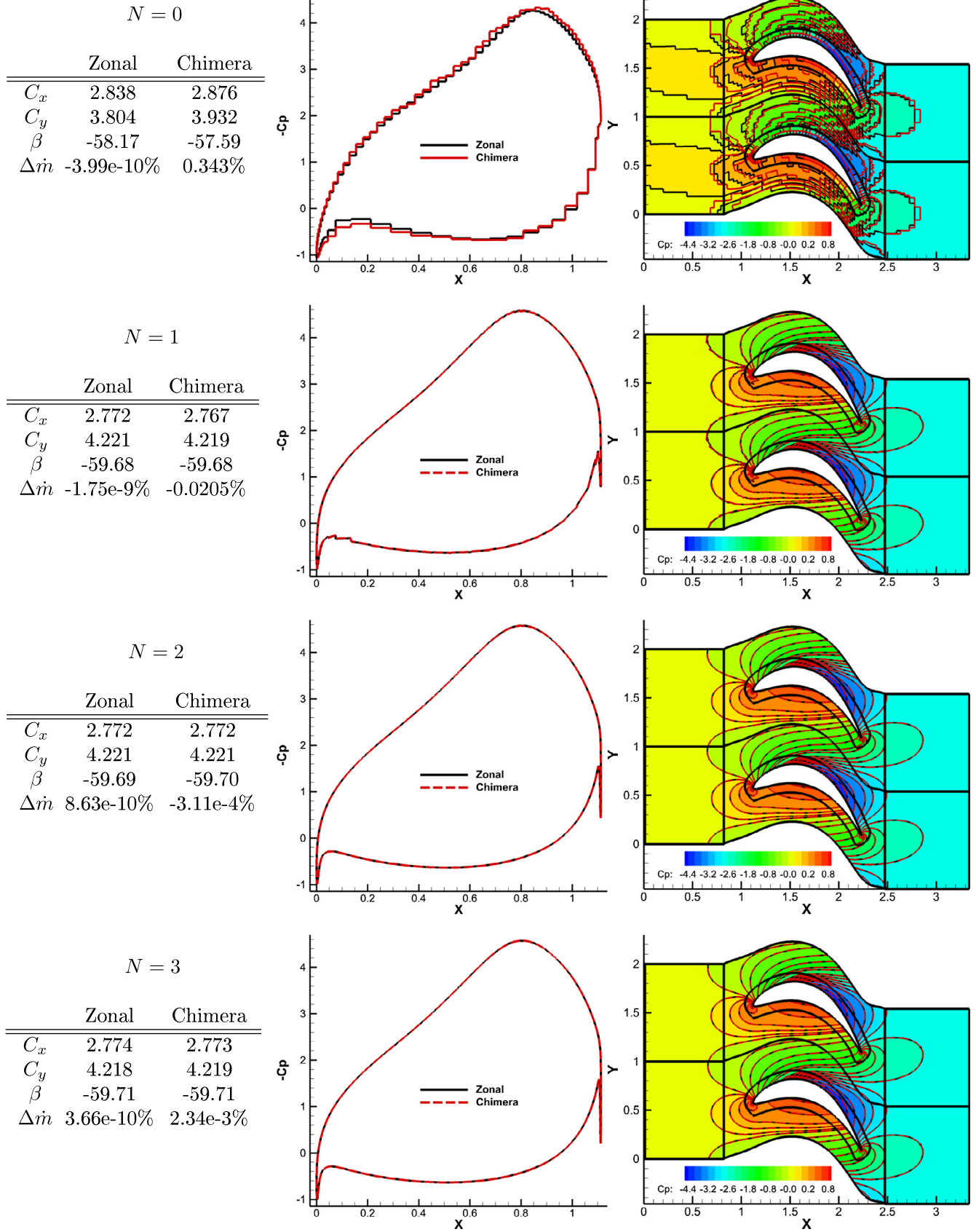
$N = 0$

	Zonal	Chimera
C_x	2.838	2.876
C_y	3.804	3.932
β	-58.17	-57.59
$\Delta\dot{m}$	-3.99e-10%	0.343%

$N = 1$

	Zonal	Chimera
C_x	2.772	2.767
C_y	4.221	4.219
β	-59.68	-59.68
$\Delta\dot{m}$	-1.75e-9%	-0.0205%

$N = 2$

	Zonal	Chimera
C_x	2.772	2.772
C_y	4.221	4.221
β	-59.69	-59.70
$\Delta\dot{m}$	8.63e-10%	-3.11e-4%

$N = 3$

	Zonal	Chimera
C_x	2.774	2.773
C_y	4.218	4.219
β	-59.71	-59.71
$\Delta\dot{m}$	3.66e-10%	2.34e-3%

Fig. 17. Turbomachinery cascade blade, ($M_\infty = 0.25$).

(a) Single Grid (60×20), $N_g = 3$ (b) Chimera Mesh (60×20), (20×7), $N_g = 3$
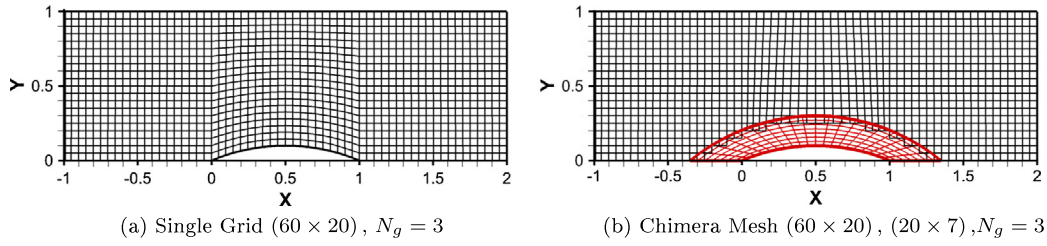
Fig. 18. Channel with 10% circular arc meshes.

$N = 0$

	$\Delta\dot{m}$
Single	2.93e-12%
Chimera	5.78e-2%

$N = 1$

	$\Delta\dot{m}$
Single	4.50e-12%
Chimera	1.30e-3%

$N = 2$

	$\Delta\dot{m}$
Single	1.90e-11%
Chimera	8.58e-3%

$N = 3$

	$\Delta\dot{m}$
Single	5.31e-12%
Chimera	1.04e-03%
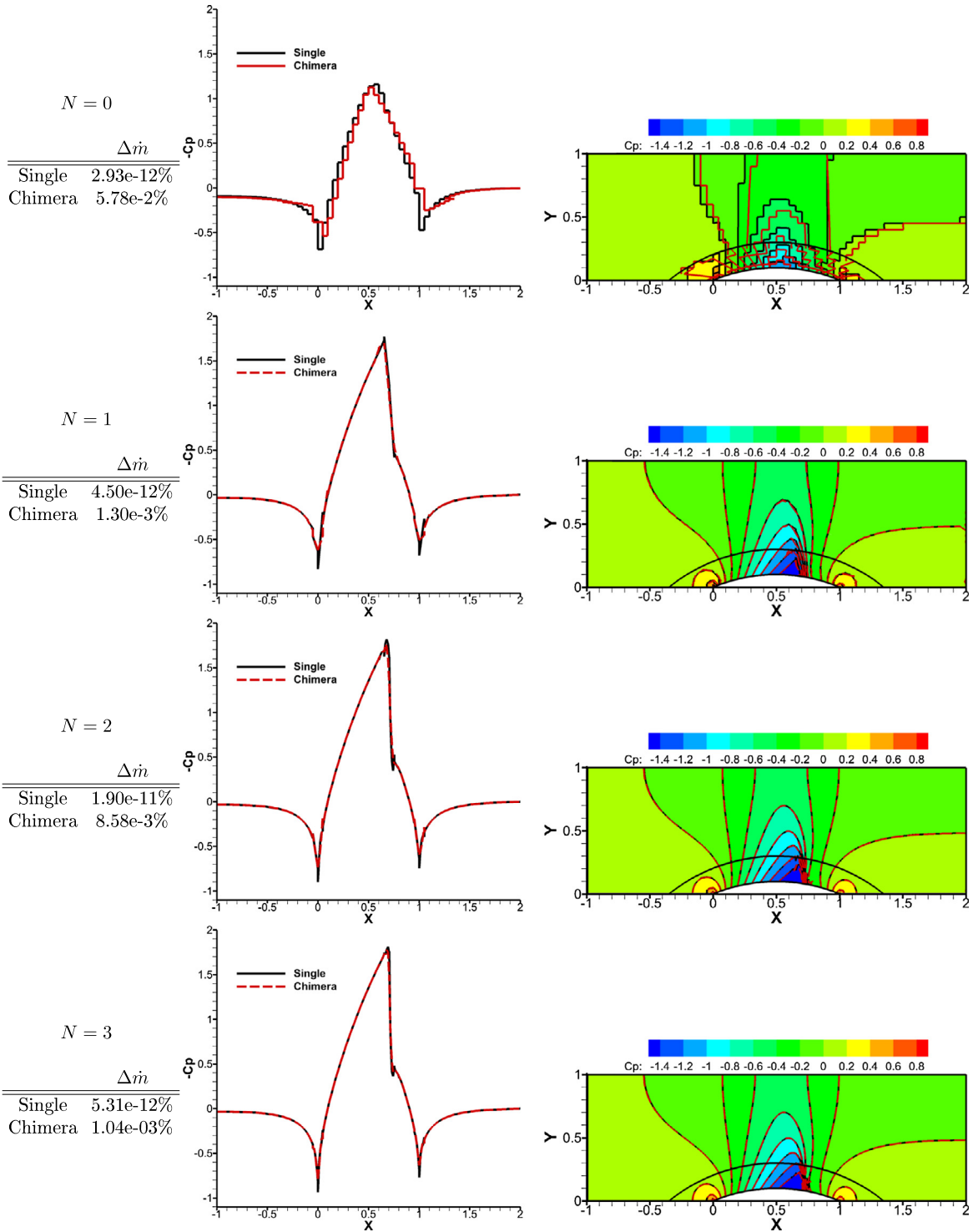
Fig. 19. Channel with 10% circular arc, $(M_\infty = 0.675)$.

(a) Single Grid(60×30), $N_g = 1$ (b) Chimera Mesh $N_g = 1$
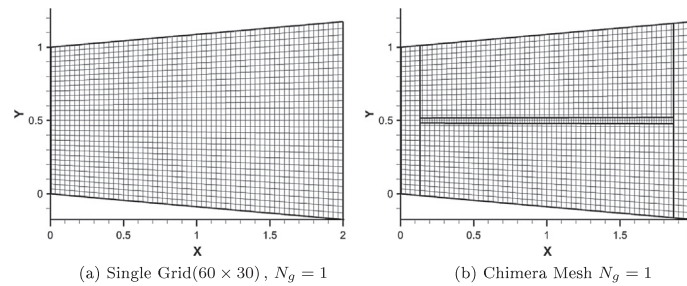
Fig. 20. Diffuser meshes.

flow and outflow is machine zero for the single grid, and tends to decrease as the order of the polynomial approximation increases. Aside from $N = 0$, the surface pressure and pressure contours agree well between the flow fields computed on the single grid and the Chimera mesh.

7.5. SKF 1.1 airfoil

The SKF 1.1 airfoil is used to demonstrate the DG-Chimera scheme on both external subsonic flow as well as external transonic flow. The three meshes used to compute the flow about the SKF 1.1 airfoil [42] are shown in Fig. 22. The first mesh in Fig. 22a is a single O-grid with a cubic cell mapping. The second mesh (Fig. 22b) is a Chimera overset mesh that uses an O-grid with a cubic cell mapping to represent the airfoil, and a second O-grid with a linear cell mapping to establish the farfield boundary 100 chords away from the airfoil. The third mesh shown in Fig. 22c is also a Chimera grid. It uses the same grid to represent the airfoil as the O-grid Chimera mesh and a rectangular background grid with a hole for the airfoil that uses a linear cell mapping. The farfield boundary is located 100 chords away from the airfoil.

For all three meshes, a slip wall boundary condition is imposed on the surface of the airfoil and a Riemann invariant condition with an angle of attack $\alpha = 2.5°$ is imposed at the farfield boundary. Two different flow fields are computed with the three meshes. The first flow field is subsonic with $M_\infty = 0.4$ and the second is transonic with a shock on the upper surface of the airfoil with $M_\infty = 0.76$. Figs. 23 and 24 show lift and drag, mass flux error, surface pressure coefficient, and pressure coefficient contours for the subsonic and transonic flow fields respectively. Lift and drag computed using the two Chimera meshes also agrees well with the values computed using the single grid for $N \geqslant 1$. The tabulated mass flux error is the mass flux integral over the farfield boundary because this is an external flow. The mass flux error for the subsonic flow field on the single grid is machine zero for all orders of the polynomial approximation, and generally decreases as the order of the polynomial approximation increases for the two Chimera meshes. Similarly the surface pressure coefficient and pressure coefficient contours agree well between the Chimera meshes and the single grid for $N \geq 1$. Notably, for $N = 3$, the stagnation pressure at the trailing edge of the airfoil nearly reaches the value of the stagnation pressure at the leading edge.

For the transonic solution, the lift and drag coefficients computed using the Chimera meshes and the single grid again agree well for $N \geq 1$. The mass flux error is near machine zero for the single grid. The increase in the mass flux error relative to the subsonic solution is a result of using the approximation in the lifting operator in the discretization of the artificial viscosity on the artificial boundaries as described in Section 5. The mass flux error generally decreases for the Chimera meshes as the order of the polynomial approximation increases. However, the mass flux error does not

decrease as rapidly compared to the subsonic flow field. While the surface pressure coefficient and pressure coefficient contours agree well between the flow fields computed on the three meshes for $N \geq 1$, small differences can be observed in the shock region. These differences can be attributed to the difference in cell size of the background grids in the two Chimera meshes and the artificial viscosity. The artificial viscosity is different on the three meshes as it is a direct function of the cell size. Away from the shock the surface pressure coefficient and pressure coefficient contours are indistinguishable between the meshes for $N \geq 2$.

7.6. Supersonic circular cylinder

This case is used to demonstrate the DG-Chimera scheme on an external supersonic flow. The three meshes used to compute the flow about a circular cylinder at $M_\infty = 2.0$ are shown in Fig. 25. The mesh in Fig. 25a is a single grid consisting of cells with a cubic polynomial mapping. The second mesh shown in Fig. 25b uses a grid with 13 cells normal to the surface and a cubic polynomial mapping to represent the surface of the cylinder. Two C-grids consisting of linearly mapped cells are used for the farfield. The set of cells on the outflow plane from the single grid are also retained from the single grid in order to form a boundary on the computational domain without overlapping cells. The third mesh (Fig. 25c) is constructed from the second but replaces the grid furthest away from the cylinder with a rectangular grid with a hole. A slip wall boundary condition is imposed on the surface of the cylinder, and freestream values are imposed on all conservative variables on the farfield boundary. All conservative variables are extrapolated on the $x = 0$ boundary.

Lift and drag coefficients, mass flux error, as well as surface pressures and contours of pressure coefficient for increasing order of the approximation are shown in Fig. 26. As the flow is symmetric, the lift coefficient is zero for all computed flow fields. The drag coefficient also agrees well between the flow fields computed using Chimera meshes and the single grid. The mass flux error is computed as the integral over the inflow and outflow boundaries. The mass flux error is machine zero for the single grid calculations. The mass flux error initially increases from $N = 0$ to $N = 1$ for the Chimera meshes. The mass flux error decreases as the order of the approximation is further increased. Again, the mass flux error does not decrease as rapidly relative to the subsonic flows. The surface pressure coefficients agree well for $N = 0$, and the pressure coefficient contours computed using the single grid and C-Grid also agree well for all orders of approximation. A slight difference between the surface pressure coefficient computed with the R-Grid relative the other two meshes for $N \geq 1$. These differences are primarily a result of differing grid resolution in the R-Grid when compared to the other two meshes. Most importantly, for both Chimera meshes, the shock is able to seamlessly pass over the artificial boundary.
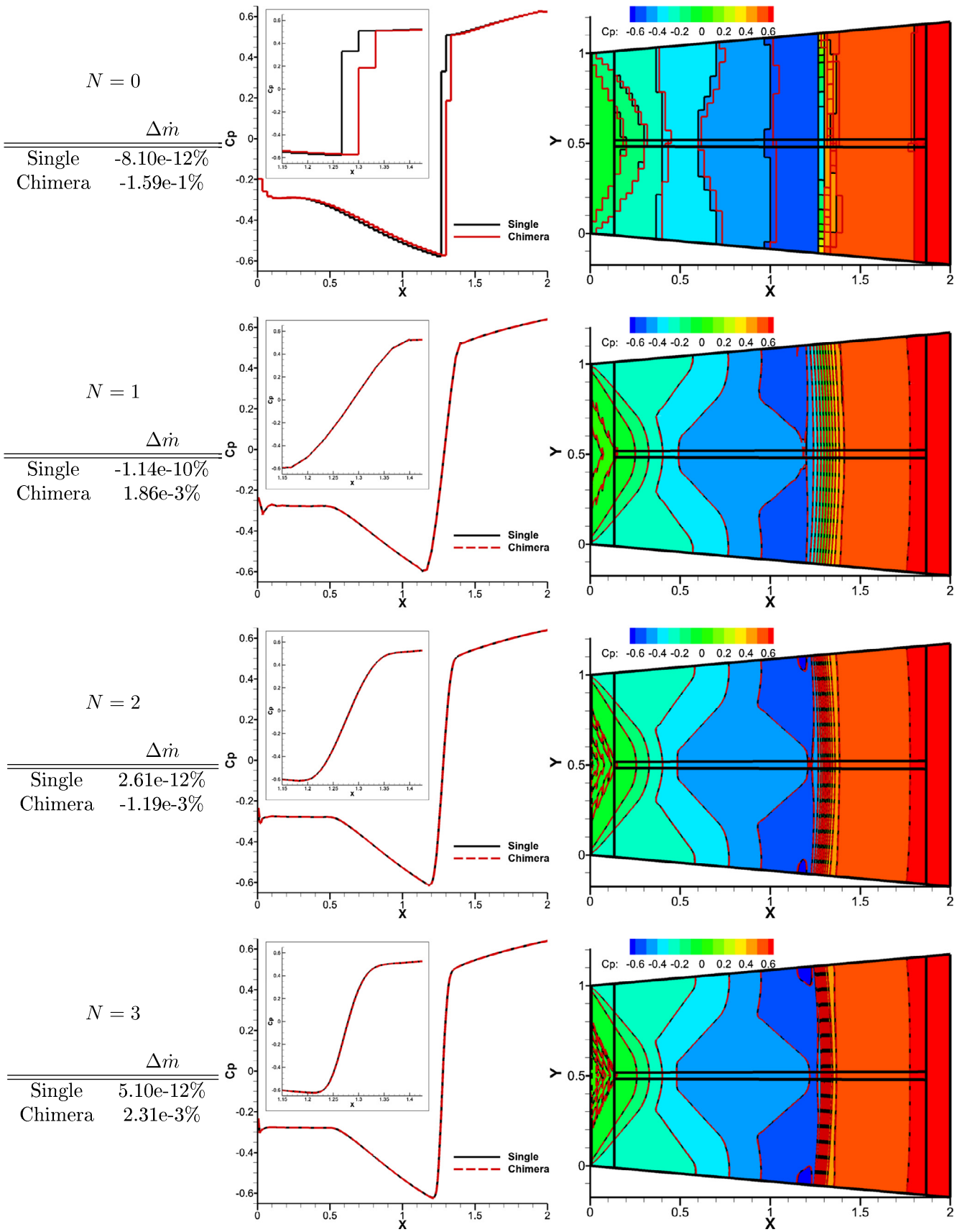
$N = 0$

	$\Delta\dot{m}$
Single	-8.10e-12%
Chimera	-1.59e-1%

$N = 1$

	$\Delta\dot{m}$
Single	-1.14e-10%
Chimera	1.86e-3%

$N = 2$

	$\Delta\dot{m}$
Single	2.61e-12%
Chimera	-1.19e-3%

$N = 3$

	$\Delta\dot{m}$
Single	5.10e-12%
Chimera	2.31e-3%

Fig. 21. Normal shock pressure coefficient.

(a) Single Grid (105×30), $N_g = 3$

(b) Chimera O-Grid Mesh (105×14), $N_g = 3$, (104×16), $N_g = 1$

(c) Chimera R-Grid Mesh (105×14), $N_g = 3$, (104×104), $N_g = 1$
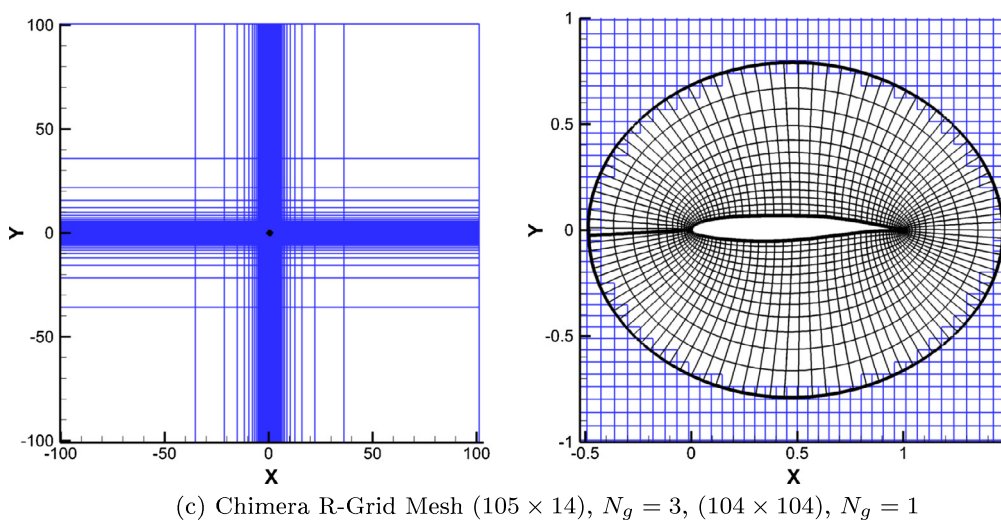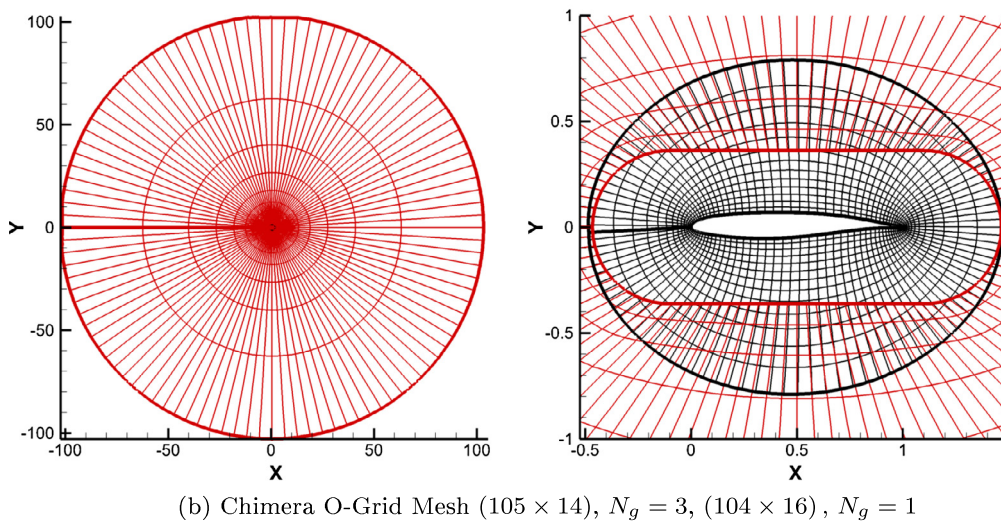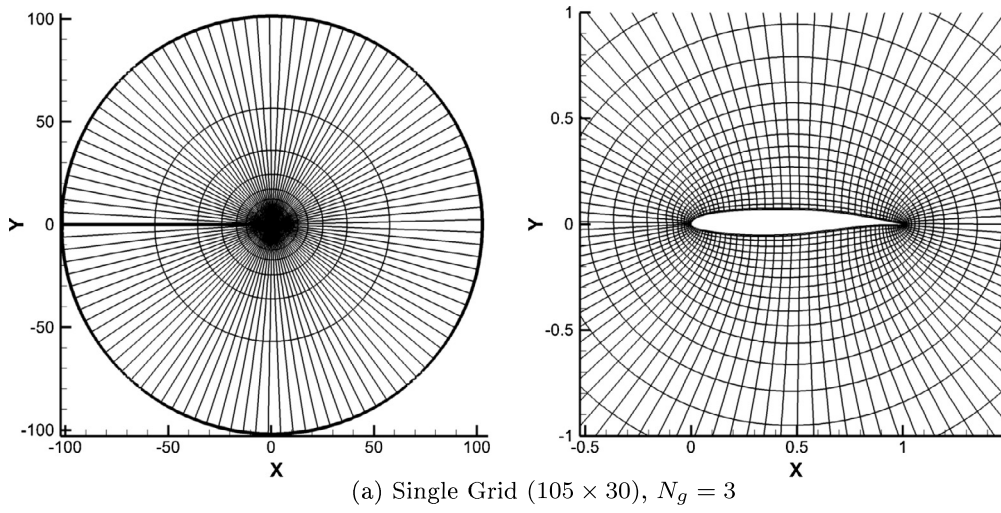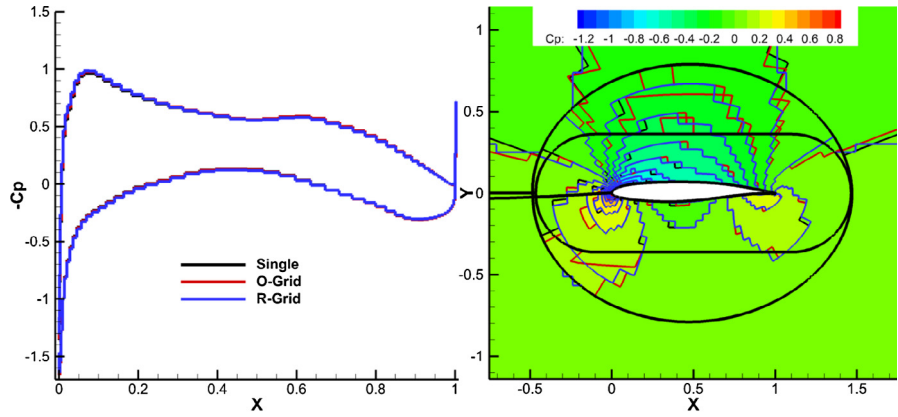
Fig. 22. SKF 1.1 airfoil meshes.

$N = 0$

	C_l	C_d	$\Delta \dot{m}$
Single	0.6389	5.82e-2	5.22e-14
O-Grid	0.6478	5.79e-2	-1.93e-3
R-Grid	0.6485	5.59e-2	2.61e-4

$N = 1$

	C_l	C_d	$\Delta \dot{m}$
Single	0.7649	1.35e-3	-7.38e-12
O-Grid	0.7645	1.35e-3	4.63e-5
R-Grid	0.7647	1.34e-3	-2.71e-5
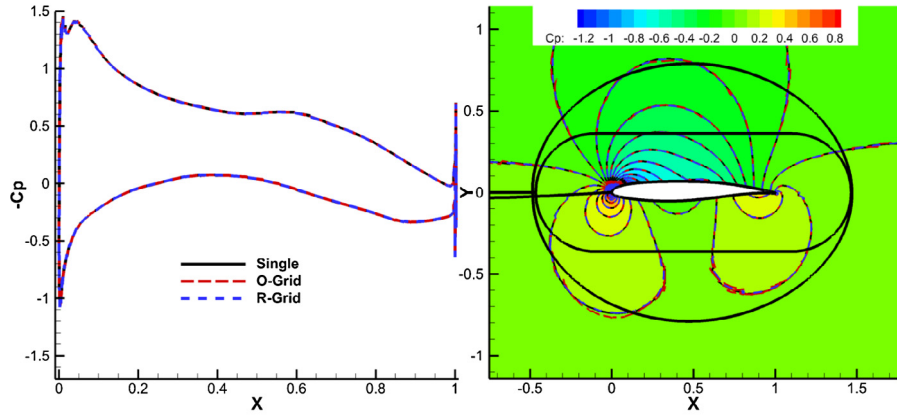
$N = 2$

	C_l	C_d	$\Delta \dot{m}$
Single	0.7670	4.01e-4	-7.61e-12
O-Grid	0.7670	3.98e-4	1.39e-8
R-Grid	0.7672	3.81e-4	3.07e-6
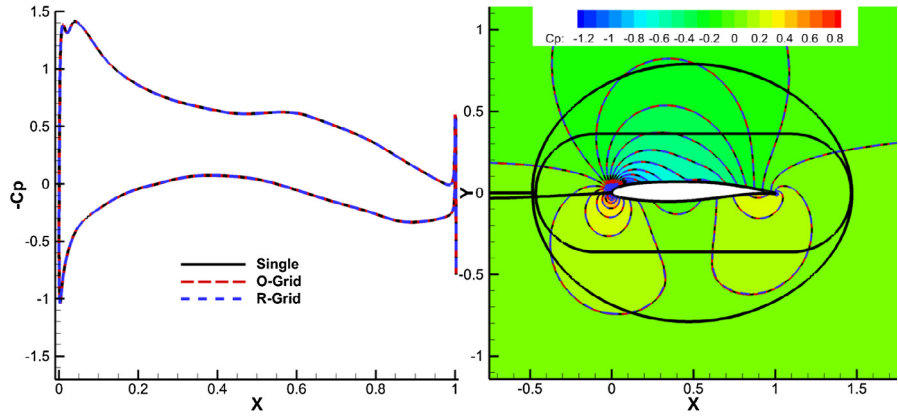
$N = 3$

	C_l	C_d	$\Delta \dot{m}$
Single	0.7615	2.86e-4	-7.76e-12
O-Grid	0.7615	2.84e-4	1.23e-6
R-Grid	0.7617	2.63e-4	-6.53e-7
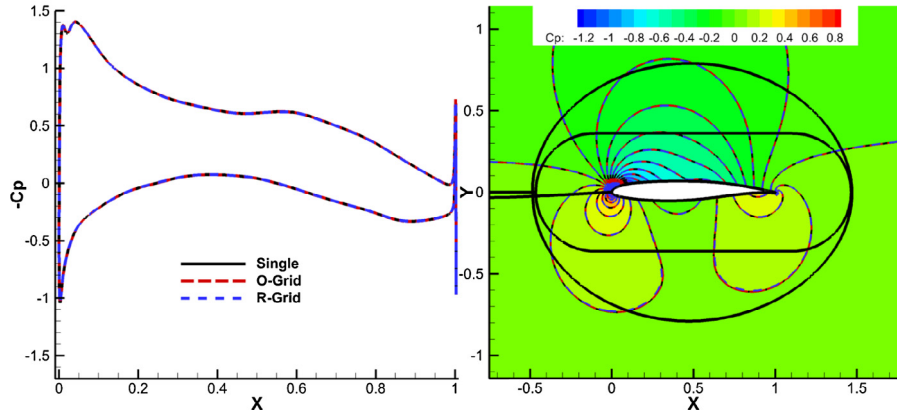
Fig. 23. SKF 1.1 airfoil, ($M_\infty = 0.4$, $\alpha = 2.5°$).

$N = 0$

	C_l	C_d	$\Delta\dot{m}$
Single	0.8864	8.76e-2	2.18e-13
O-Grid	0.9038	9.02e-2	-9.41e-3
R-Grid	0.9509	8.74e-2	4.75e-3
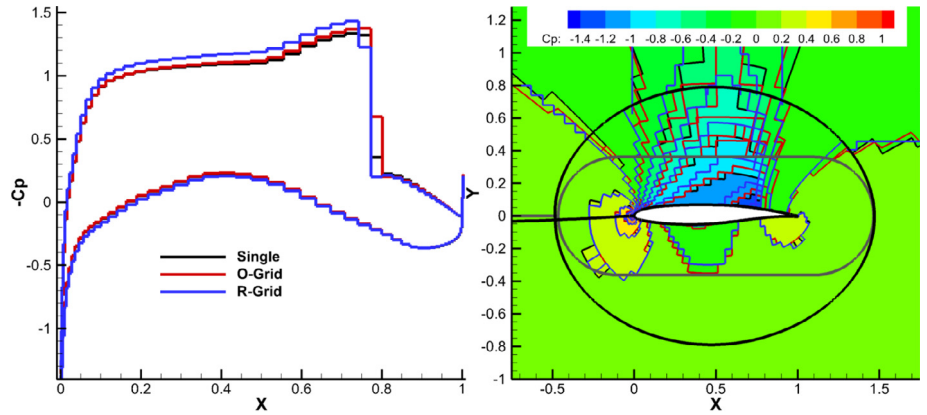
$N = 1$

	C_l	C_d	$\Delta\dot{m}$
Single	1.0533	6.40e-2	-4.08e-7
O-Grid	1.0477	6.26e-2	4.46e-4
R-Grid	1.0591	6.50e-2	-8.07e-4
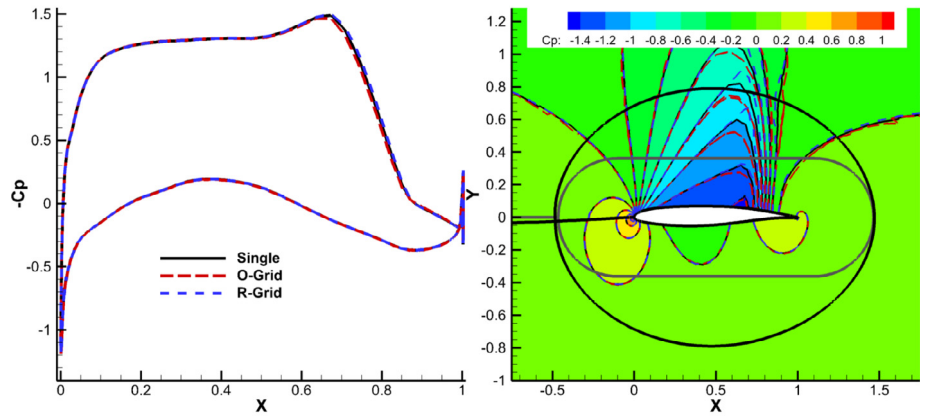
$N = 2$

	C_l	C_d	$\Delta\dot{m}$
Single	1.0472	6.00e-2	9.32e-7
O-Grid	1.0435	5.91e-2	6.35e-4
R-Grid	1.0498	6.05e-2	-4.30e-4
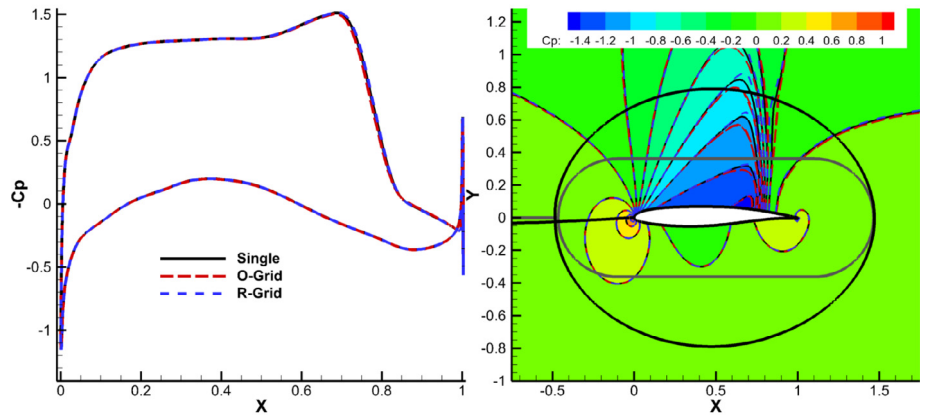
$N = 3$

	C_l	C_d	$\Delta\dot{m}$
Single	1.0461	5.86e-2	5.79e-7
O-Grid	1.0442	5.81e-2	2.71e-4
R-Grid	1.0478	5.89e-2	-1.63e-4
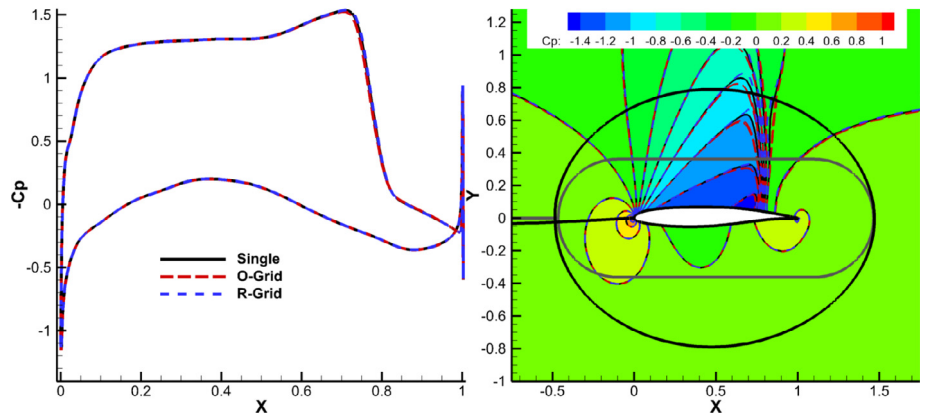
Fig. 24. SKF 1.1 airfoil, ($M_\infty = 0.76$, $\alpha = 2.5°$).

(a) Single Grid (56×35), $N_g = 3$

(b) Multiple C-Grids (56×13), $N_g = 3$, $2 \times (1 \times 22)$, $N_g = 3$, (56×19), $N_g = 1$, (56×3), $N_g = 1$

(c) Multiple C-Grids with a Rectangular Grid (R-Grid) (56×13), $N_g = 3$, $2 \times (1 \times 22)$, $N_g = 3$, (56×14), $N_g = 1$, (34×70), $N_g = 1$
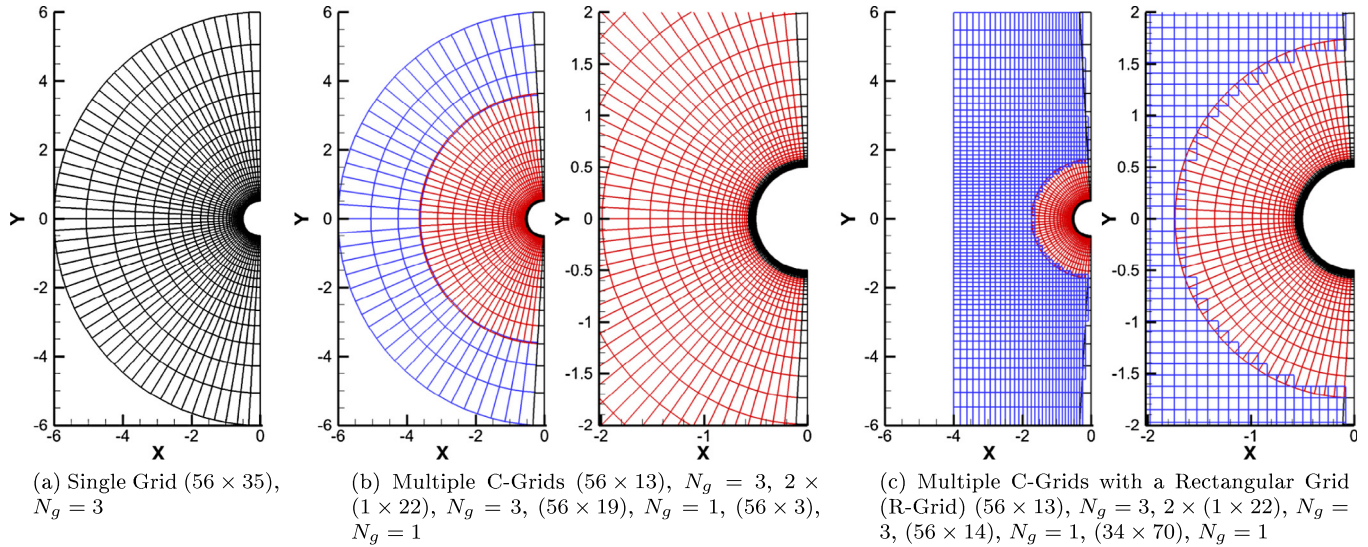
Fig. 25. Supersonic inviscid cylinder meshes, ($M_\infty = 2.0$).

7.7. SKF 1.1 airfoil with flap

The geometry for the SKF 1.1 airfoil with the flap extended is shown in Fig. 27a (see, configuration 5 in Ref. [42]. This geometry is used to demonstrate a traditional use of Chimera grids to mesh complex configurations [1]. A zonal mesh [39] consisting of two grids using a cubic polynomial mapping, $N_g = 3$. without any overlapping regions is shown in Fig. 27b and c. The mesh consists of a grid that wraps around both the airfoil and the flap, and a second grid that spans the gap between the airfoil and flap as shown in Fig. 27c. The farfield boundary is located 100 chords away from the airfoil. A Chimera overset mesh consisting of 3 grids, one for the airfoil with $N_g = 3$, one for the flap with $N_g = 3$, and one which extends the farfield to 100 chords from the airfoil with $N_g = 1$, is shown in Fig. 27d. The surface of the airfoil is used to cut a hole in the flap grid, and the surface of the flap is used to cut a hole in the airfoil grid. The hole cut by the flap is shown in Fig. 27e, and the hole cut by the airfoil is shown in Fig. 27f. The hole cutting results in artificial boundaries with significant disparity in cell sizes between donor and receiver cells as shown in Fig. 27g.

The inviscid flow field is computed about the SKF 1.1 airfoil with the flap using the zonal and Chimera meshes. The farfield boundary is imposed using a Riemann invariant boundary condition with $M_\infty = 0.2$ and $\alpha = 3°$, and the airfoil surface boundary condition is a slip wall boundary condition. Lift, drag, mass flux error, surface pressure coefficient, and pressure coefficient contours for the two meshes are shown with increasing order of the approximation polynomial in Fig. 28. Lift and drag computed using the two meshes agree well for $N \geqslant 1$. The mass flux error is computed as the integral of the farfield boundary. The zonal mesh has a machine zero mass flux error for all orders of approximation, and the mass flux error for the Chimera mesh decreases with an increase in the order of approximation. The surface pressure and pressure contours computed using the two meshes agrees well for $N \geqslant 1$. Hence, the Chimera mesh is able to obtain solutions of similar quality of the zonal mesh.

7.8. Isentropic convecting vortex

The DG-Chimera scheme is applied to an inviscid problem consisting of a compressible vortex convecting in a rectangular

domain with periodic conditions imposed on all sides [50–52]. This flow problem demonstrates the benefits of high-order accurate schemes with low dissipation. The vortex is initially positioned at $(x_0, y_0) = (0.05, 0.05)$ and convects with the free-stream for 12 characteristic time units where it returns to its starting position. The analytical solution is given by

$$f(x,y,t) = \left(1 - ((x - x_0) - |V_\infty|cos(\theta)t)^2 - ((y - y_0) - |V_\infty|sin(\theta)t)^2\right)/r_c^2$$

$$u_v(x,y,t) = |V_\infty|\left(cos(\theta) - \frac{\epsilon((y - y_0) - |V_\infty|sin(\theta)t)}{2\pi r_c}exp\left(\frac{f(x,y,t)}{2}\right)\right)$$

$$v_v(x,y,t) = |V_\infty|\left(sin(\theta) + \frac{\epsilon((x - x_0) - |V_\infty|cos(\theta)t)}{2\pi r_c}exp\left(\frac{f(x,y,t)}{2}\right)\right)$$

$$\rho_v(x,y,t) = \rho_\infty\left(1 - \frac{\epsilon^2(\gamma - 1)M_\infty^2}{8\pi^2}exp(f(x,y,t))\right)^{\frac{1}{\gamma-1}}$$

$$p_v(x,y,t) = p_\infty\left(1 - \frac{\epsilon^2(\gamma - 1)M_\infty^2}{8\pi^2}exp(f(x,y,t))\right)^{\frac{\gamma}{\gamma-1}} \quad (26)$$

where θ is the flow angle, ϵ is a measure of the strength of the vortex, and r_c is a measure of the size of the vortex. Solutions are obtained using $M_\infty = 0.5$, $\epsilon = 1$, $r_c = 0.005$, and $\theta = 0$. The vortex is advanced in time with a time step of $\Delta t = 0.005$ using the unsteady Euler equations in Eq. (1) that are discretized with a 3rd-order accurate three stage Diagonally Implicit Runge–Kutta (DIRK) [53] scheme. The implicit system of equations associated with each stage of the DIRK scheme is solved with a Newton's method that is converged until the L^2-norm of the residual vector drops below a tolerance of 5×10^{-10}.

The initial vortex location on the four meshes used to convect the vortex are shown in Fig. 29. The meshes consist of a background grid and a wavy grid that cuts a hole in the background grid. The wavy grid is formed by perturbing the coordinates from a uniform square grid using the formula

$$x_w = x + L_s 0.04 sin(2\pi(y - y_s)/L_s)$$
$$y_w = y + L_s 0.04 sin(2\pi(x - x_s)/L_s), \quad (27)$$

where $L_s = 0.058$ is the height and width of the square and (x_s, y_s) is the lower left hand corner of the square. The cell count in each
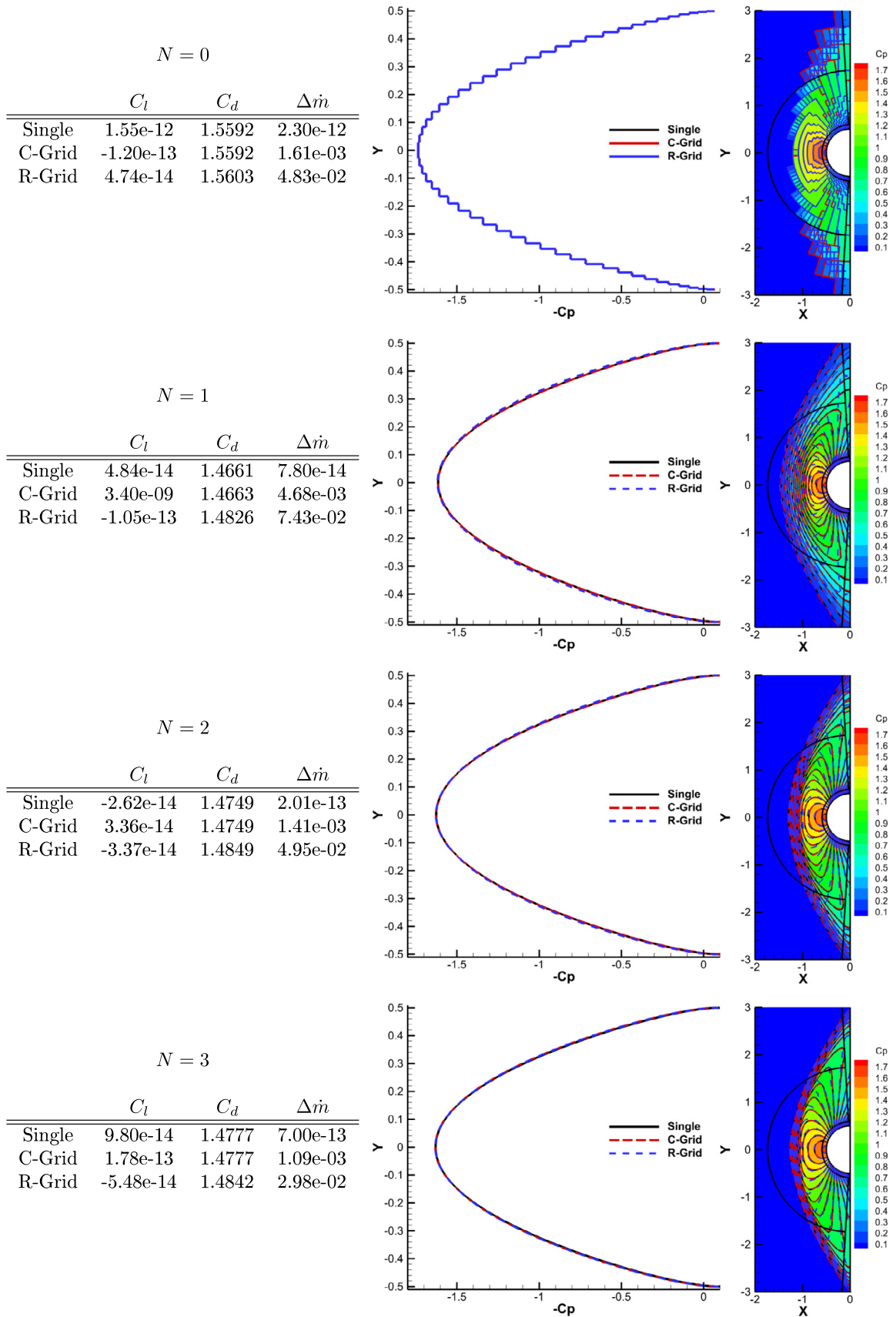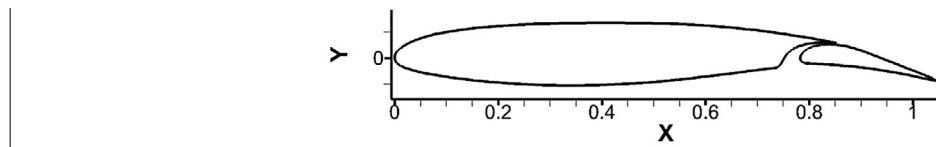
$N = 0$

	C_l	C_d	$\Delta\dot{m}$
Single	1.55e-12	1.5592	2.30e-12
C-Grid	-1.20e-13	1.5592	1.61e-03
R-Grid	4.74e-14	1.5603	4.83e-02

$N = 1$

	C_l	C_d	$\Delta\dot{m}$
Single	4.84e-14	1.4661	7.80e-14
C-Grid	3.40e-09	1.4663	4.68e-03
R-Grid	-1.05e-13	1.4826	7.43e-02

$N = 2$

	C_l	C_d	$\Delta\dot{m}$
Single	-2.62e-14	1.4749	2.01e-13
C-Grid	3.36e-14	1.4749	1.41e-03
R-Grid	-3.37e-14	1.4849	4.95e-02

$N = 3$

	C_l	C_d	$\Delta\dot{m}$
Single	9.80e-14	1.4777	7.00e-13
C-Grid	1.78e-13	1.4777	1.09e-03
R-Grid	-5.48e-14	1.4842	2.98e-02

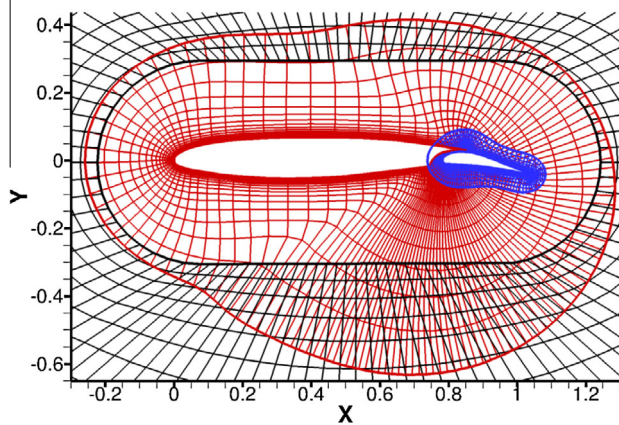**Fig. 26.** Circular cylinder pressure coefficient, ($M_\infty = 2$).
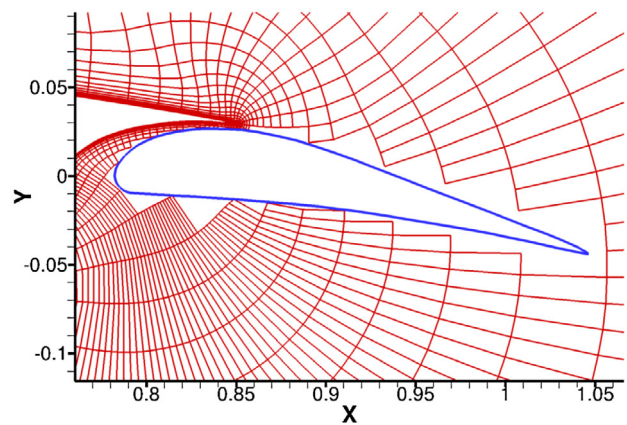
(a) SKF 1.1 Airfoil with Flap Geometry
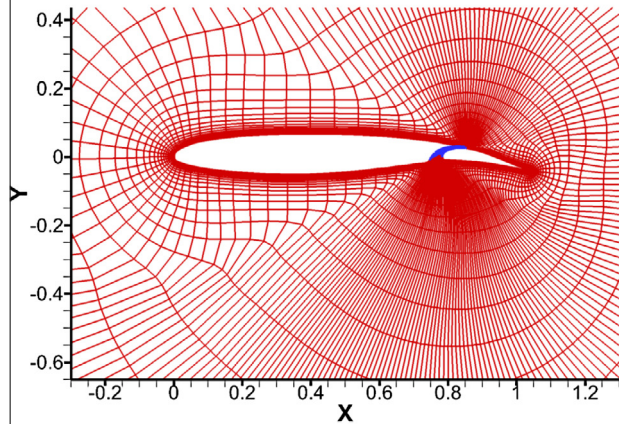
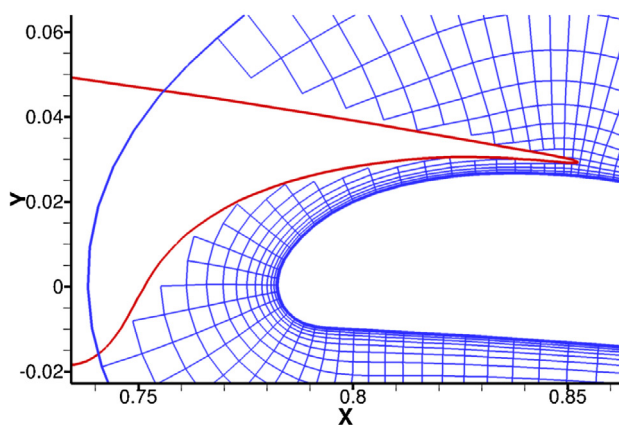(b) SKF 1.1 Airfoil with Flap Zonal Mesh
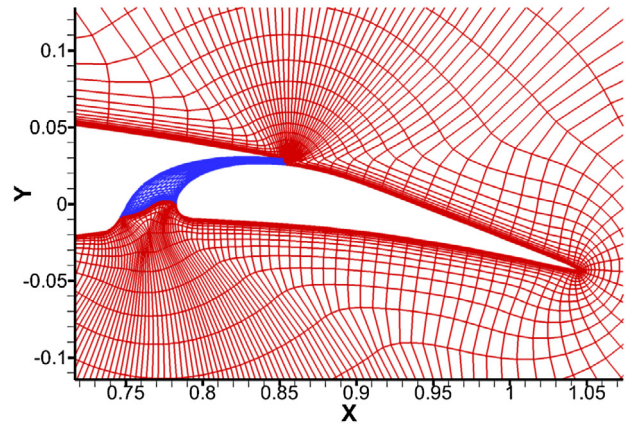
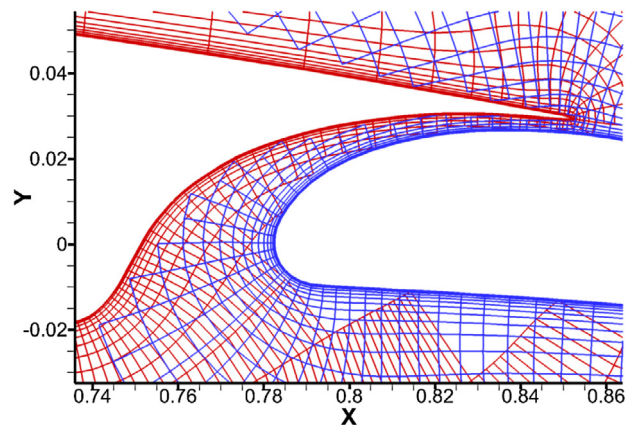(c) Closeup of Zonal Mesh around the Flap

(d) SKF 1.1 Airfoil with Flap Overset Mesh with Hole Cuts

(e) Hole Cut from Airfoil Grid using the Flap Surface

(f) Hole Cut from Flap Grid using the Airfoil Surface

(g) Closeup of Chimera Mesh around the Flap

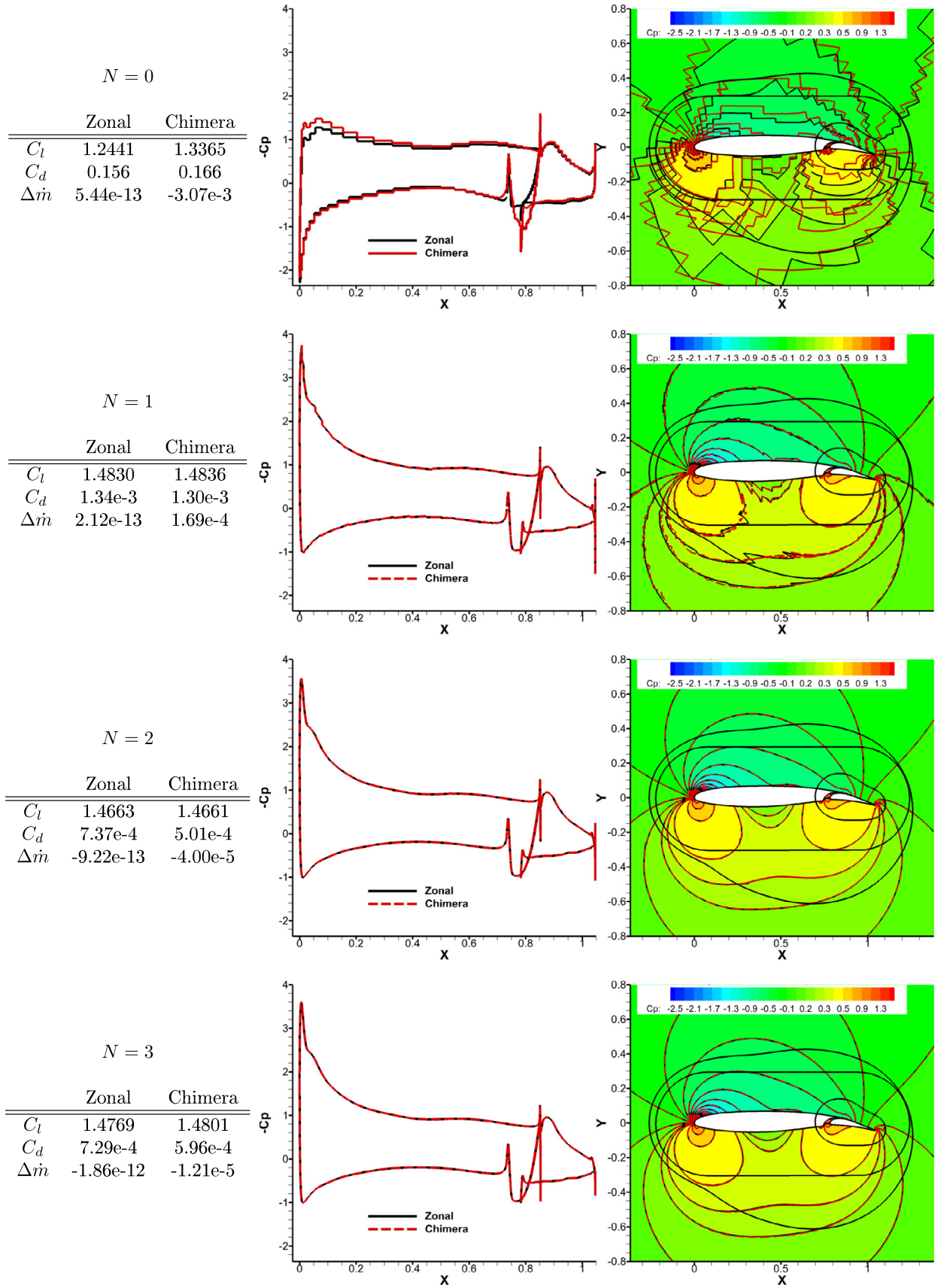**Fig. 27.** SKF 1.1 airfoil with flap meshes.

$N = 0$

	Zonal	Chimera
C_l	1.2441	1.3365
C_d	0.156	0.166
$\Delta\dot{m}$	5.44e-13	-3.07e-3

$N = 1$

	Zonal	Chimera
C_l	1.4830	1.4836
C_d	1.34e-3	1.30e-3
$\Delta\dot{m}$	2.12e-13	1.69e-4

$N = 2$

	Zonal	Chimera
C_l	1.4663	1.4661
C_d	7.37e-4	5.01e-4
$\Delta\dot{m}$	-9.22e-13	-4.00e-5

$N = 3$

	Zonal	Chimera
C_l	1.4769	1.4801
C_d	7.29e-4	5.96e-4
$\Delta\dot{m}$	-1.86e-12	-1.21e-5

Fig. 28. SKF 1.1 airfoil with flap pressure coefficient, ($M_\infty = 0.2$, $\alpha = 3°$).

(a) Mesh for $N = 0$, (396×132), (84×84), $N_g = 1$

(b) Mesh for $N = 1$, (198×66), (42×42), $N_g = 1$

(c) Mesh for $N = 2$, (132×44), (28×28), $N_g = 1$

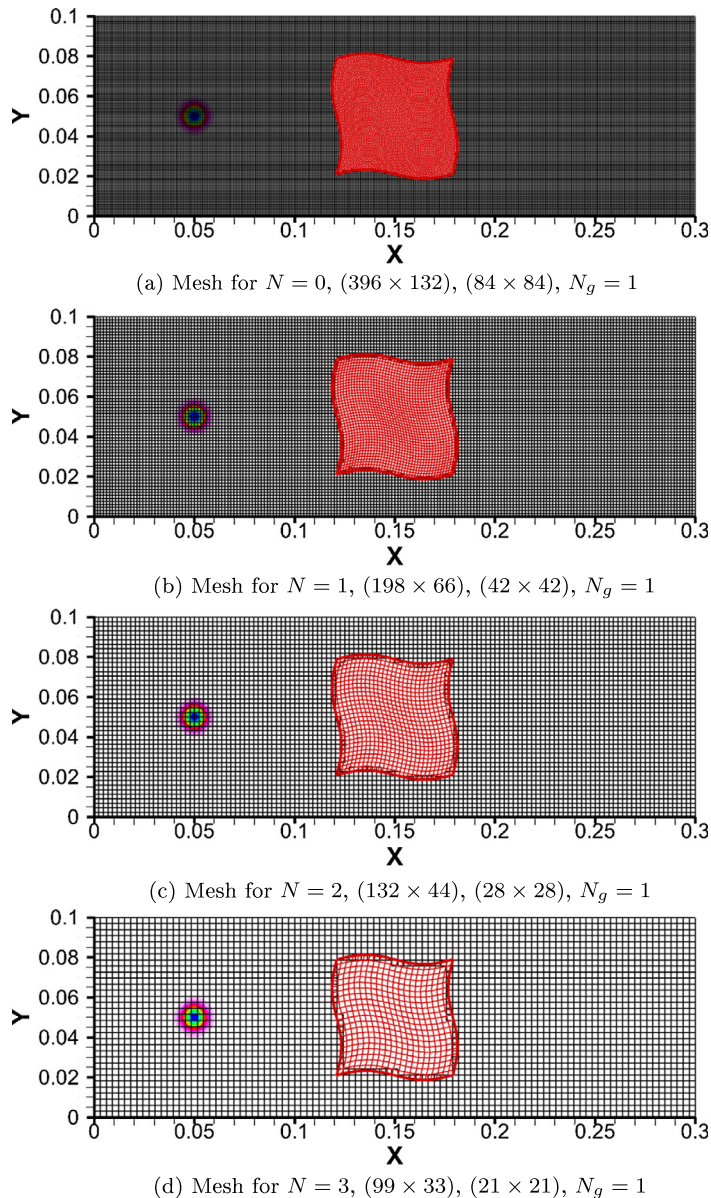(d) Mesh for $N = 3$, (99×33), (21×21), $N_g = 1$

Fig. 29. Isentropic convecting vortex meshes, $(M_\infty = 0.5)$.

mesh decreases as the order of the polynomial approximation is increased such that the total number of degrees of freedom remains a constant 52,272 in the background grid and 7056 in the wavy grid. The vortex is also convected on the background grid without the presence of the wave grid to assess the influence of the artificial boundaries.

The pressure coefficient along the horizontal centerline and pressure coefficient contours at the initial time and final time of $t = 12$ is shown in Fig. 30. The entropy rise defined as

$$Entropy\ Rise = \frac{\frac{p}{\rho^\gamma} - \frac{p_\infty}{\rho_\infty^\gamma}}{\frac{p_\infty}{\rho_\infty^\gamma}}, \tag{28}$$

along the horizontal centerline is also shown in Fig. 30. The vortex for the 1st-order accurate, $N = 0$, solution dissipates within the first characteristic time. As a result, the solution at $t = 12$ is nearly a uniform stream solution. The 2nd-order accurate solution, $N = 1$, has maintained the vortex, though it has dissipated significantly and

is asymmetric on the horizontal centerline. It is difficult to discern the vortex in the pressure coefficient contours. The 3rd-order accurate solution, $N = 2$, has preserved the pressure deficit associated with the vortex well. The magnitude of the pressure deficit has only a relatively small amount. The pressure coefficient contours at $t = 12$ also agree well with the initial condition. The 4th-order solution, $N = 3$, at $t = 12$ also agrees well with the initial condition in the horizontal centerline pressure and the pressure contours. As expected, the entropy error decreases as the order of the polynomial approximation increases. Notably, the solutions on the single grid and the Chimera mesh agree well in both pressure coefficient and entropy error for $N \geq 1$. This indicates that the artificial boundaries do not introduce a significant error and the vortex is able to convect at the correct speed across the wavy grid in the Chimera mesh. These results also demonstrate that the low dissipation associated with high-order discretization is able to maintain the vortex over a longer period of time for a given number of degrees of freedom.
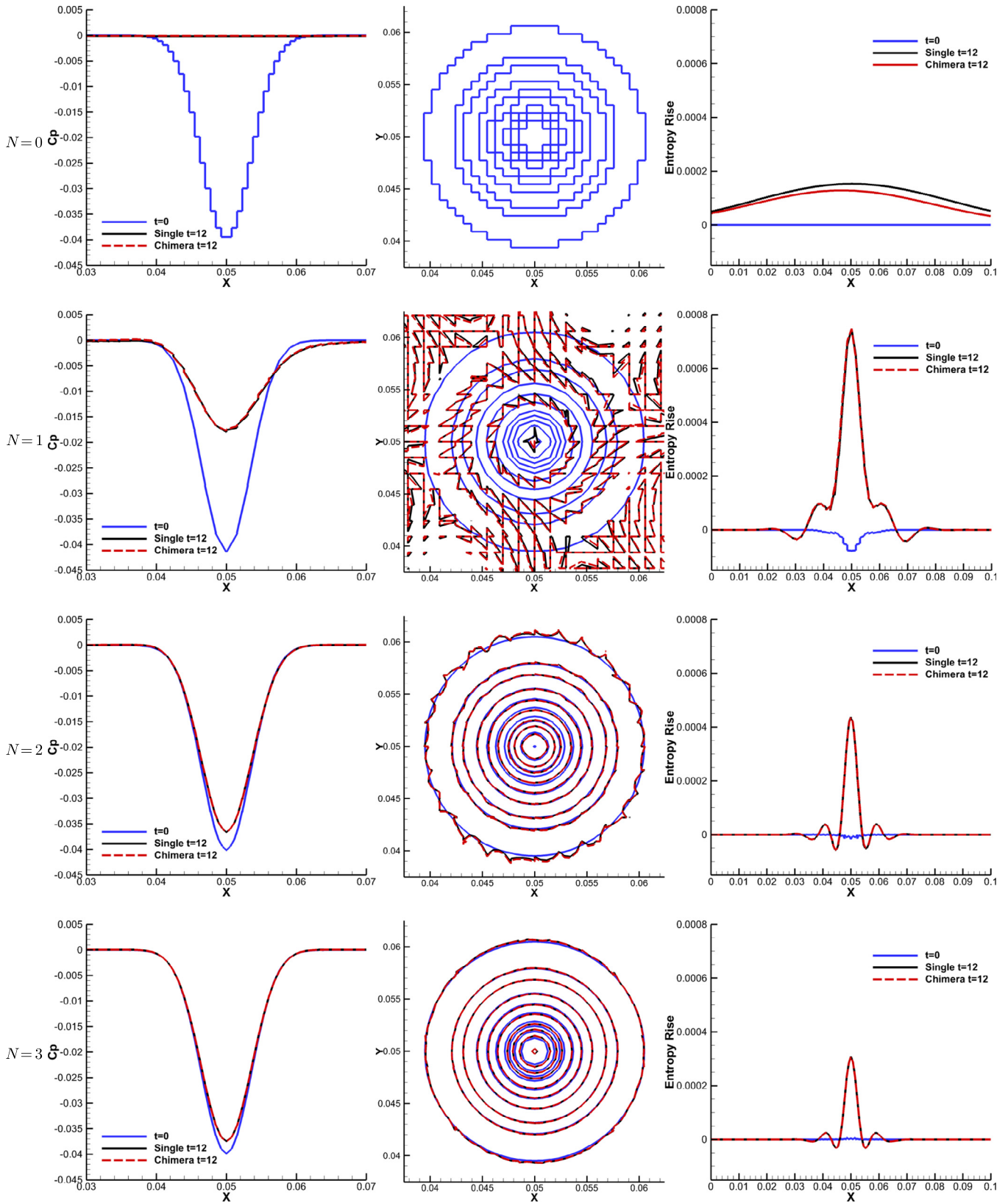
Fig. 30. Convecting isentropic vortex after 12 characteristic times, $(M_\infty = 0.5)$.

8. Conclusion

A DG-Chimera scheme has been developed and demonstrated on a set of inviscid subsonic, transonic, and supersonic internal and external flow problems. The scheme does not require the use of fringe points in order to maintain the interior DG discretization scheme across inter-grid communication boundaries. Hence, proper communication between grids can be established so long as artificial

boundaries overlap or abut neighboring grids, and the scheme naturally reduces to a zonal scheme for abutting grids without any additional logic. The inter-grid communication scheme relies on the cell local DG polynomial approximation to interpolate information and hence does not require an interpolation scheme with a large stencil. This feature further simplifies the inter-grid communication scheme and hole cutting procedures relative to traditional finite volume and finite difference Chimera schemes. The DG-Chimera scheme readily extends to three-dimensions and is expected to greatly simplify grid generation as grids can be generated without regard to fringe points or interpolation stencils.

Inviscid channel flow demonstrated that the numerical mass flux errors associated with the artificial boundaries are consistent for all orders of accuracy and small for $N \geq 1$. The mass flux error associated with the artificial boundaries is reduced by using a Gauss-Quadrature node count of $N_{GQ} = \lceil 3N/2 \rceil + 1$. Even though the mass flux errors are small, their presences does suggest exploration of methods that can reduce or eliminate these errors and are also extensible to three-dimensions is warranted.

Inviscid internal and external subsonic, transonic, and supersonic flow fields obtained using Chimera overset meshes agree well with flow fields obtained using a single grid with comparable mesh resolution for $N \geq 1$. Notably, the DG-Chimera scheme is able to transfer strong gradients, such as shocks, across artificial boundaries. The scheme was used to compute the inviscid flow about the SKF 1.1. airfoil with a flap; a flow problem that represents traditional use of the Chimera method to represent complex geometry. The convection of an isentropic vortex demonstrates that the 3rd-order and 4th-order DG schemes are able to maintain the pressure deficit associated with the vortex without significant dissipation for a fixed number of degrees of freedom relative to the 1st-order and 2nd-order DG schemes. The artificial boundary did not introduce significant errors in the time accurate calculation.

Acknowledgments

References

[1] Benek JA, Steger JL, Dougherty FC. A flexible grid embedding technique with application to the euler equations. AIAA-Paper 1983-1944; 1983.
[2] Chan WM. Overset grid technology development at NASA Ames Research Center. Comput Fluids 2009;38:496–503.
[3] Lijewski LE, Suhs NE. Time-accurate computational fluid dynamics approach to transonic store separation trajectory prediction. J Aircraft 1994;31(4):886–91.
[4] Wang ZJ. A conservative interface algorithm for moving chimera (overlapped) grids. Int J Comput Fluid Dyn 1998;10(3):255–65.
[5] Pomin H, Wagner S. Aeroelastic analysis of helicopter rotor blades on deformable chimera grids. J Aircraft 2004;41(3):577–84.
[6] Sitaraman J, Potsdam M, Wissink A, Jayaraman B, Datta A, Mavriplis D, et al. Rotor loads prediction using helios: a multisolver framework for rotorcraft aeromechanics analysis. J Aircraft 2013;50(2):478–92.
[7] Chao J, Haselbacher A, Balachandar S. A massively parallel multi-block hybrid compact-weno scheme for compressible flows. J Comput Phys 2009;228:7473–91.
[8] Rizzi A, Eliasson P, Lindblad I, Hirsch C, Lacor C, Haeuser J. The engineering of multiblock/multigrid software for Navier–Stokes flows on structured meshes. Comput Fluids 1993;22:341–67.
[9] Rogers SE, Suhs NE, Dietz WE, Nash SM, Onufer JT. PEGASUS user's guide version 5.1 k. NASA Ames Research Center; Micro Craft; MCAT, Inc; 2003. http://people.nas.nasa.gov/rogers/pegasus/uguide.html.
[10] Rogers SE, Suhs NE, Dietz WE. Pegasus 5: an automated preprocessor for overset-grid computational fluid dynamics. AIAA J 2003;41(6):1037–45.
[11] Visbal MR, Gaitonde DV. High-order-accurate methods for complex unsteady subsonic flows. AIAA J 1999;37(10):1231–9.
[12] Rizzetta DP, Visbal MR. Numerical simulation of separation control for transitional highly loaded low-pressure turbines. AIAA J 2005;43(9):1958–67.
[13] Georgiadis N, Rizzetta D, Fureby C. Large-eddy simulation: current capabilities, recommended practices, and future research. AIAA J 2010;48(8):1772–84.
[14] Sherer SE, Visbal MR, Gordnier RE, Yilmaz TO, Rockwell DO. 1303 unmanned combat air vehicle flowfield simulations and comparison with experimental data. J Aircraft 2011;48(3):1005–19.
[15] Wang Z, Fidkowski K, Abgrall R, Bassi F, Caraeni D, Cary A, et al. High-order cfd methods: current status and perspective. Int J Numer Methods Fluids 2012;00:1–42. http://dx.doi.org/10.1002/fld.3767.
[16] Lele SA. Compact finite difference schemes with spectral-like resolution. J Comput Phys 1992;103(1):16–42.
[17] Liu X-D, Osher S, Chan T. Weighted essentially non-oscillatory schemes. J Comput Phys 1994;115(1):200–12.
[18] Jiang G-S, Shu C-W. Efficient implementation of weighted eno schemes. J Comput Phys 1996;126(1):202–28.
[19] Sherer SE, Scott JN. High-order compact finite-difference methods on general overset grids. J Comput Phys 2005;210(2):459–96.
[20] Sherer ES, Visbal MR, Galbraith MC. Automated preprocessing tools for use with a higher-order overset-grid algorithm. AIAA Paper 2006-1147; January 2006.
[21] Sherer SE. Investigation of high-order and optimized interpolation methods with implementation in a high-order overset grid fluid dynamics solver. PhD thesis. The Ohio State University; 2002.
[22] Reed WH, Hill TR. Triangular mesh methods for the neutron transport equation. Tech Rep LA-UR-73-479. Los Alamos Scientific Laboratory; 1973.
[23] Cockburn B, Shu C-W. Tvb runge-kutta local projection discontinuous Galerkin finite element method for conservation laws ii: general framework. Math Comput 1989;52(186):411–35.
[24] Wang ZJ, Hariharan N, Chen R. Recent development on the conservation property of chimera. Int J Comput Fluid Dyn 2001;15(4):265–78.
[25] Wang ZJ, Buning PG, Benek JA. Critical evaluation of conservative and non-conservative interface treatment for chimera grids. AIAA-Paper 1995-0077; 1995.
[26] Wang ZJ, Yang HQ. A unified conservative zonal interface treatment for arbitrarily patched and overlapped grids. AIAA-Paper 1994-0320; 1994.
[27] Moon YJ, Liou M-S. Conservative treatment of boundary interfaces for overlaid grids and multi-level grid adaptations. AIAA-Paper 1989-1980-CP; 1989.
[28] Cali PM, Couaillier V. Conservative interfacing for overset grids. AIAA-Paper 2000-1008; 2000.
[29] Meakin RL. On the spatial and temporal accuracy of overset grid methods for moving body problems. AIAA-Paper 1994-1925; 1994.
[30] Barter GE. Shock capturing with pde-based artificial viscosity for an adaptive, higher-order discontinuous Galerkin finite element method. PhD thesis. Massachusetts Institute of Technology; June 2008.
[31] Barter GE, Darmofal DL. Shock capturing with pde-based artificial viscosity for dgfem: Part 1. Formulation. J Comput Phys 2010;229(5):1810–27.
[32] Burgess NK. An adaptive discontinuous Galerkin solver for aerodynamic flows. PhD thesis. University of Wyoming; November 2011.
[33] Persson P-O, Peraire J. Sub-cell shock capturing for discontinuous Galerkin methods. AIAA-Paper 2006-112; 2006.
[34] Abramowitz M, Stegun IA. Handbook of mathematical functions with formulas, graphs, and mathematical tables. New York: Dover; 1965.
[35] Roe PL. Approximate riemann solvers, parameter vectors, and difference schemes. J Comput Phys 1981;43:357–72.
[36] Bassi F, Rebay S, Mariotti G, Pedinotti S, Savini M. A high-order accurate discontinuous finite element method for inviscid and viscous turbomachinery flows. In: 2nd European conference on turbomachinery fluid dynamics and thermodynamics. Technologisch Instituut, Antwerpen, Belgium; 1997. p. 99–108.
[37] Galbraith MC, Orkwis PD, Benek JA. Automated quadrature-free discontinuous Galerkin method applied to viscous flows. AIAA-Paper 2011-493; 2011.
[38] de Berg M, Cheong O, van Kreveld M. Computational geometry: algorithms and applications. 3rd ed. Springer; 2008.
[39] Rai MM. An implicit, conservative, zonal-boundary scheme for euler equation calculations. Comput Fluids 1986;14:295–319.
[40] Orkwis PD, McRae DS. Newton's method solver for high-speed viscous separated flowfields. AIAA J 1992;30:78–85.
[41] Saad Y. Iterative methods for sparse linear systems. 2nd ed. SIAM; 2000.
[42] Stanewsky E, Thibert JJ. Airfoil skf 1.1 with maneuver flap. Tech rep. Experimental Data Base for Computer Program Assessment, AGARD-AR-138; 1979.
[43] Bassi F, Rebay S. High-order accurate discontinuous finite element solution of the 2d euler equations. J Comput Phys 1997;138:251–85.
[44] Fidkowski KJ, Oliver TA, Lu J, Darmofal DL. p-Multigrid solutions of high-order discontinuous Galerkin discretizations of the compressible Navier–Stokes equations. J Comput Phys 2005;207:92–113.
[45] Mattingly HD, Heiser WH, Pratt DT. Aircraft engine design. 2nd ed. AIAA Education Series; 2002.
[46] Dixon SL, Hall C. Fluid mechanics and thermodynamics of turbomachinery. 6th ed. Elsevier; 2010.
[47] Galbraith MC, Orkwis PD, Benek JA. Hole cutting of curved discontinuous Galerkin chimera overset meshes using a direct cut method. AIAA-Paper 2013-2428; 2013.

[48] Ni R. A multiple grid scheme for solving the euler equations. In: Computational fluid dynamics conference, 5th, Palo Alto, Calif, June 22, 23, 1981. Collection of technical papers, vol. 1. New York: American Institute of Aeronautics and Astronautics, Inc.; 1981. p. 257–64 (A81-37526 16-34).

[49] Anderson JD. Modern compressible flow: with historical perspective. 3rd ed. McGraw-Hill; 2003.

[50] Erlebacher G, Hussaini MY, Shu C-W. Interaction of a shock with a longitudinal vortex. J Fluid Mech 1997;337:129–53.

[51] Mattsson K, Svard M, Carpenter M, Nordstrom J. High-order accurate computations for unsteady aerodynamics. Comput Fluids 2007;36(3):636–49.

[52] Persson PO, Bonet J, Peraire J. Discontinuous Galerkin solution of the Navier–Stokes equations on deformable domains. Cmput Methods Appl Mech Eng 2009;198(17–20):1585–95.

[53] Alexander R. Diagonally implicit Runge–Kutta methods for stiff ode's. SIAM J Numer Anal 1977;14(6):1006–21.